Eberhard Karl University of Tübingen
Institute for Astronomy and Astrophysics (IAAT)

Modeling Reflection Spectra from Returning Radiation in X-ray Binaries

MSc. Astro and Particle Physics

Master Thesis

Supervisors
Prof. Konstantinos Kokkotas
Prof. Andrea Santangelo

Graduate Student
Konstantinos Kourmpetis

Tübingen, April 1 2026

Declaration of Originality

Hereby I confirm, Konstantinos Kourmpetis, Matr. Nr. 7051986, that this assignment is my own work and that I have only sought and used mentioned tools. I have clearly referenced in the text and the bibliography all sources used in the work (printed sources, internet or any other source), including verbatim citations or paraphrases. I am aware of the fact that plagiarism is an attempt to deceit which, in case of recurrence, can result in a loss of test authorization. Furthermore, I confirm that neither this work nor parts of it have been previously, or concurrently, used as an exam work – neither for other courses nor within other exam processes.

Place and date ___________________________ Signature _________________

Abstract

X-ray reflection spectroscopy is a powerful tool to explore the innermost regions of accreting black holes, test General Relativity in the strong-field regime, and most importantly, measure the spin of black holes. The X-ray spectra of black hole X-ray binaries usually consist of three main components: thermal emission from the accretion disk, Comptonized emission from a hot corona, and a reflection component resulting from the illumination of the disk by the corona. In the disk's rest frame, the reflection spectrum shows fluorescent emission lines and a broad Compton hump, peaking between 20 and 40 keV. The most notable spectral line is generally the iron Kα complex, which appears at 6.4 keV for neutral or weakly ionized iron, and shifts up to 6.97 keV for fully ionized, hydrogen-like iron. Modeling these signatures provides key information about the black hole's spin and disk's parameters. A phenomenon known as returning radiation, light from the disk that is bent back onto it by the black hole's strong gravity, can significantly affect disk illumination, especially for rapidly rotating black holes in the soft spectral state. Nevertheless, this effect is often neglected or treated approximately in current reflection models implemented in the XSPEC fitting software. In this work, we present `zijiRetRad`, a new reflection model that, for the first time, self-consistently incorporates returning radiation. To isolate this effect, we adopt the standard disk-corona configuration but disable the corona, allowing the reflection spectrum to be produced solely by self-irradiation of the disk. When applied to the X-ray binary 4U 1630–47, the model yields a rapidly spinning black hole ($a_* > 0.98$), consistent with previous studies. Compared to the existing models, `zijiRetRad` naturally produces a harder high-energy reflection spectrum, without invoking a Comptonized component.

Related Publication

Kostas Kourmpetis, Shafqat Riaz, Honghui Liu, Temurbek Mirzaev, Cosimo Bambi, Debtroy Das, Jiachen Jiang, Kostas D. Kokkotas, and Andrea Santangelo, *Modeling X-Ray reflection spectra from returning radiation: application to 4U 1630–47*, arXiv:2601.14860, 2026.

To my parents, for always supporting my dreams.

Acknowledgements

I am deeply grateful to Shafqat Riaz and Honghui Liu for their constant supervision, guidance, and support throughout this thesis. You were always there to answer my endless (and often strange) questions, and your patience and encouragement made this work possible. I truly appreciate everything I learned from you.

I would also like to thank Prof. Kostas Kokkotas and Prof. Andrea Santangelo for their continuous support, both scientifically and professionally. From discussions to conference opportunities, you were always there for me. I greatly enjoyed being part of both your groups.

A special thank you goes to Prof. Kokkotas, Heike and the TAT group, with whom I spent most of my time during this thesis. You made me feel at home from day one. Coming to the office was always a pleasure rather than a duty. Arthur, Marta, and Jose, thank you for the endless physics discussions, whether in the office or at the bar. I learned a great deal from all of you. I would also like to thank my friend Marta for carefully reading this thesis and providing valuable feedback.

I am also grateful to Prof. Cosimo Bambi for carefully reviewing the results of this thesis and offering insightful comments and suggestions. Moreover, I would like to thank Temurbek Mirzaev for patiently answering my numerous emails and questions regarding the code used in this work, and Debtroy Das for his valuable insights regarding the source 4U 1639–47.

I want to thank my dear friends back in Greece; Alex, Moschos, Telis, as well as my brother Dimitris, for always being there for me. Despite the distance and our different lives, your regular calls and support meant a lot. I would also like to thank my dear Zina for her love, patience, and support throughout this journey. Finally, a heartfelt thank you to my parents for always supporting even my wildest dreams. This thesis is for you.

Last but not least, I would like to thank Mr. Athanasios Martinos for his generous financial support during my Master's studies. None of this would have been possible without your help.

Contents

Chapter 1

Introduction & Motivation

In black hole X-ray binary (XRB) systems, a companion star transfers matter onto a stellar-mass black hole, forming an accretion disk that emits strongly in the X-rays (Shakura and Sunyaev, 1973; Novikov and K. S. Thorne, 1973). Determining the spin of stellar-mass black holes is crucial, as it provides insight into the collapse of massive stars and may help explain high-energy phenomena such as relativistic jets (e.g., Roger Penrose, 1969; Blandford and Znajek, 1977; A. R. King and Kolb, 1999; M. C. Miller and Jon M. Miller, 2015).

In the last decades, several techniques have been developed to measure black hole spins, including the *continuum-fitting method* (S. N. Zhang, Cui, and Chen, 1997; J. E. McClintock, Narayan, and J. F. Steiner, 2014), *X-ray reflection spectroscopy* (Fabian, Rees, et al., 1989; Christopher S. Reynolds, 2014; C. Bambi et al., 2021), *quasi-periodic oscillations* (QPOs) (S. E. Motta, T. M. Belloni, et al., 2014; S. E. Motta, Munoz-Darias, et al., 2014; A. R. Ingram and Sara E. Motta, 2019; Liu, Ji, et al., 2021), *X-ray polarimetry* (Dovčiak et al., 2008; Marra et al., 2024; James F. Steiner et al., 2024), and *gravitational-wave detections* (B. P. Abbott, R. Abbott, T. D. Abbott, Abernathy, et al., 2016; B. P. Abbott, R. Abbott, T. D. Abbott, Abraham, et al., 2019). Among these, X-ray reflection spectroscopy stands out as a particularly powerful diagnostic tool, as it probes the innermost regions of accreting systems (e.g., Fabian, Wilkins, et al., 2012; García, James F. Steiner, et al., 2015; Walton et al., 2016; Liu, Cosimo Bambi, et al., 2023; Liu, Jiachen Jiang, et al., 2023) and enables tests of General Relativity in the strong-field regime (De Rosa et al., 2019; C. S. Reynolds, 2021; C. Bambi et al., 2021; Tripathi, Y. Zhang, et al., 2021; Tripathi, Nampalliwar, et al., 2019; Liu, Askar B. Abdikamalov, et al., 2019; Liu, H. Wang, et al., 2020).

In this framework, a primary X-ray source irradiates the accretion disk, producing a reflection spectrum that carries distinctive reflection features shaped by Doppler shifts, gravitational redshift, and light bending. Since these effects depend sensitively on the location of the disk's inner edge, commonly associated with the innermost stable circular orbit (ISCO or $R_{\rm isco}$), modeling the reflection spectrum allows one to infer the black hole spin.

Despite significant progress in X-ray reflection modeling over the past years, particularly with sophisticated frameworks such as `relxill` (T. Dauser, J. Garcia, et al., 2013; J. Garcia, T. Dauser, Lohfink, et al., 2014), current models still rely on several simplifying assumptions. One key approximation concerns *returning radiation*, or *self-irradiation* of the accretion disk, which refers to photons emitted by the disk that are bent back onto it by the strong gravitational field of the black hole. This effect, first calculated by C. Cunningham, 1976, is expected to be most important in the innermost regions of the accretion disk, close to the black hole. While some modern models attempt to include returning radiation, it is currently treated only approximately in the XSPEC data analysis software (T. Dauser, J. A. Garcia, et al., 2022; García, Thomas Dauser, et al., 2022).

The primary motivation of this thesis is that no XSPEC model yet exists that self-consistently accounts for returning radiation. During the soft spectral state of XRBs, where the thermal component dominates and the accretion disk extends down to the ISCO, the self-irradiation of the disk is expected to be particularly significant, potentially producing novel observational signatures in the reflection spectrum. In this thesis, we adapt the current state-of-the-art returning radiation code presented by T. Mirzaev, C. Bambi, et al., 2024 and implement it in XSPEC as a fully self-consistent model. We then test the validity of our model by fitting it to observational data, discuss the results and their implications, and assess the significance of returning radiation in real XRB systems.

This thesis is organized as follows. In Chapter 2, we present the necessary theoretical background to understand the physics underlying X-ray reflection spectroscopy and black hole accretion. Chapter 3 describes the development and implementation of a new XSPEC model, along with a discussion of the results. Finally, Chapter 4 summarizes the conclusions and suggests directions for future work.

Chapter 2

Theoretical Background

This chapter introduces the theoretical framework required for this thesis. Understanding X-ray reflection spectroscopy requires a description of black holes, the spacetime around them, the structure of accretion disks, and the physical processes responsible for the observed reflection features. The chapter is organized as follows. We first introduce black holes as compact objects and discuss their basic properties. We then describe the Kerr spacetime, which provides the framework for modeling the motion of matter around rotating black holes. Next, we present the Novikov-Thorne accretion disk model adopted in this work. Finally, we introduce the method of X-ray reflection spectroscopy and the physical processes responsible for the observed reflection features.

2.1 Black Holes

In simple terms, a black hole is a region of spacetime where gravity is so strong that nothing can escape, not even light. The idea of such extremely compact objects is far from new. In 1783, John Michell, and independently in 1796, Pierre-Simon Laplace, considered this possibility within a Newtonian framework, calling them "dark stars". To escape a gravitational field, a particle must reach a velocity greater than the so-called escape velocity, which depends on the compact object's mass. For comparison, the escape velocity at the surface of Earth is about 11 km/s; fast enough to leave our planet, but tiny compared to the speed of light. In the extreme case where the escape velocity equals the speed of light, nothing can escape, giving rise to what we now call a black hole. This classical picture of black holes is simplistic and rather naive, but it provides an intuitive way to understand the underlying concept.

Modern physics places black holes firmly within the framework of General Relativity, proposed by Albert Einstein in 1915 (Einstein, 1916). As John Wheeler famously summarized: "space-time tells matter how to move; matter tells spacetime how to curve". Just a year later, Karl Schwarzschild found the first exact solution of Einstein's field equations describing a non-rotating black hole (Schwarzschild, 1916). Its deeper physical meaning, including the presence of an event horizon, was understood only in 1958, when David Finkelstein recognized that it causally separates the interior from the outside universe (Finkelstein, 1958). It took almost 50 years before the rotating black hole solution was derived, in 1963, by Roy Kerr; the solution that now provides the framework for modeling astrophysical black holes (Kerr, 1963).

Astrophysical black holes remained controversial for decades. If they exist, they must form when massive stars collapse under their own gravity after exhausting nuclear fuel, a scenario that Arthur Eddington famously dismissed as "absurd", insisting that "there should be a law of nature to prevent a star from behaving in this absurd way". The idea of real black holes gained traction in 1964, when Yakov Zel'dovich and, independently, Edwin Salpeter proposed that quasars are powered by supermassive black holes (Zel'dovich, 1964; Salpeter, 1964). The first stellar-mass black hole candidate, Cygnus X-1, was identified in 1972 by Thomas Bolton and, independently, Louise Webster and Paul Murdin; a true breakthrough in observational astrophysics (Bolton, 1972; Webster and Murdin, 1972).

Since then, several observations have confirmed the existence of both stellar-mass black holes in XRBs (Remillard and Jeffrey E. McClintock, 2006) and supermassive black holes at galactic centers (Kormendy and Richstone, 1995). The discovery of gravitational waves from merging black holes by LIGO in 2015 (B. P. Abbott, R. Abbott, T. D. Abbott, Abernathy, et al., 2016) and the first image of a black hole by the Event Horizon Telescope in 2019 (Event Horizon Telescope Collaboration, Akiyama, Alberdi, Alef, Asada, et al., 2019) have opened entirely new windows on these fascinating objects.

In this section, we introduce black holes within the context of General Relativity and discuss the black hole classes observed in the universe, with a focus on XRBs. This section is adapted from Cosimo Bambi, 2018a and Chapter 1 of C. Bambi, 2017.

2.1.1 Black Holes in General Relativity

To introduce black holes within General Relativity, we begin with the Einstein field equations:

$$G_{\mu\nu} = \kappa T_{\mu\nu}, \tag{2.1}$$

where $G_{\mu\nu}$ is the Einstein tensor, $T_{\mu\nu}$ is the energy-momentum tensor, and $\kappa = 8\pi G/c^4$, with G the gravitational constant. The Einstein tensor is given by:

$$G_{\mu\nu} = R_{\mu\nu} - \frac{1}{2} R g_{\mu\nu}, \tag{2.2}$$

where $R_{\mu\nu}$ is the Ricci curvature tensor and R is the Ricci scalar.

The left-hand side of the Einstein field equations is purely geometrical, encoding the curvature of spacetime, while the right-hand side describes the energy and momentum content of matter and radiation. In this way, the Einstein equations establish a direct relationship between spacetime geometry and matter: the distribution of energy and momentum determines the curvature of spacetime, which in turn governs the motion of matter and radiation.

Black holes arise as vacuum solutions of the Einstein field equations:

$$G_{\mu\nu} = 0, \tag{2.3}$$

corresponding to a vanishing energy-momentum tensor, $T_{\mu\nu} = 0$. Formally, using the framework introduced by Penrose for studying causality in asymptotically flat spacetimes (R. Penrose, 1965), a black hole can be defined as follows (C. Bambi, 2017):

> A black hole in an asymptotically flat spacetime $\mathscr{M}$ is the set of events that do not belong to the causal past of the future null infinity $J^-(\mathscr{S}^+)$, namely:
>
> $$\mathscr{B} = \mathscr{M} - J^-(\mathscr{P}^+) \neq \emptyset. \tag{2.4}$$
>
> The event horizon is the boundary of region $\mathscr{B}$.

The future null infinity ($\mathscr{P}^+$), represents the "destination" of outgoing light rays that escape to infinity. The causal past of a region $\mathscr{P}$, denoted as $J^-(\mathscr{P}^+)$, is the set of all events that can influence $\mathscr{P}$. A black hole region, $\mathscr{B}$, is then defined as the set of events that do not belong to the causal past of future null infinity. In other words, anything inside $\mathscr{B}$ cannot send signals to distant observers. Its boundary, the *event horizon*, acts as a one-way membrane: once an object crosses it, no signal from that object can reach the exterior universe.

According to the *no-hair theorem* (Israel, 1967; Carter, 1971; Hawking, 1972), black holes in General Relativity are completely characterized by only three macroscopic parameters: their mass M, angular momentum J, and electric charge Q. Under appropriate assumptions, including stationarity, asymptotic flatness, and the absence of naked singularities, these parameters uniquely determine the black hole spacetime.

For a given set of symmetries and physical properties, the Einstein field equations admit unique black hole solutions. In particular, *Birkhoff's theorem* states that any spherically symmetric vacuum solution of the Einstein equations is described by the Schwarzschild metric (Birkhoff and Langer, 1923; Jebsen, 1921). Consequently, a non-rotating and uncharged black hole is uniquely described by the Schwarzschild solution (Schwarzschild, 1916). Including electric charge leads to the Reissner-Nordström solution (Reissner, 1916; Nordström, 1918), while allowing for rotation results in the Kerr solution (Kerr, 1963). The most general stationary, asymptotically flat black hole solution in General Relativity, characterized by mass, angular momentum, and charge, is given by the Kerr-Newman metric (Newman et al., 1965). Although the Kerr-Newman solution represents the most general case, astrophysical black holes are expected to carry negligible electric charge, as any net charge would be rapidly neutralized by the surrounding plasma. As a result, realistic astrophysical black holes are well described by the Kerr metric, an assumption commonly referred to as the *Kerr hypothesis*.

2.1.2 Astrophysical Black Holes

Observationally, astrophysical black holes are commonly classified into three categories:

1. stellar-mass black holes,
2. supermassive black holes,
3. intermediate-mass black holes.

From the perspective of General Relativity, there are no constraints on the mass of a black hole, which may in principle take arbitrarily small or large values. Astrophysical considerations, however, impose strong restrictions through the available formation channels.

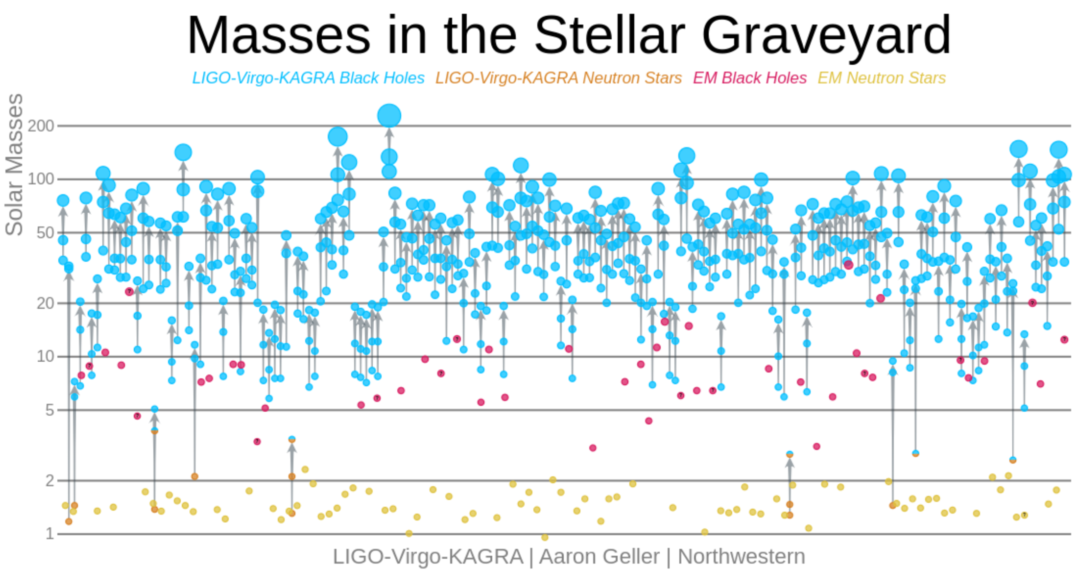

Figure 2.1: Black holes and neutron stars discovered by the LIGO-Virgo-KAGRA collaboration (blue and orange dots) until January 2024, compared to those discovered by electromagnetic (EM) means (red and yellow dots) over the last ~ 60 years. The arrows show the merging compact objects. Credit: LIGO-Virgo-KAGRA / Aaron Geller / Northwestern.

Stellar-mass black holes are formed through the collapse of massive stars, and their final masses depend sensitively on stellar evolution and supernova explosion mechanisms (Belczynski et al., 2010). A key parameter in this process is the stellar metallicity, defined as the fraction of elements heavier than helium, which strongly influences mass loss through stellar winds. Higher metallicity stars experience stronger mass loss, leading to lighter remnants, whereas low-metallicity stars can produce more massive black holes. Theoretical models predict a mass gap in the black hole remnant spectrum when considering low-metallicity progenitors, roughly between $50 - 150\,\mathrm{M}_\odot$ (Heger and Woosley, 2002; Heger, Fryer, et

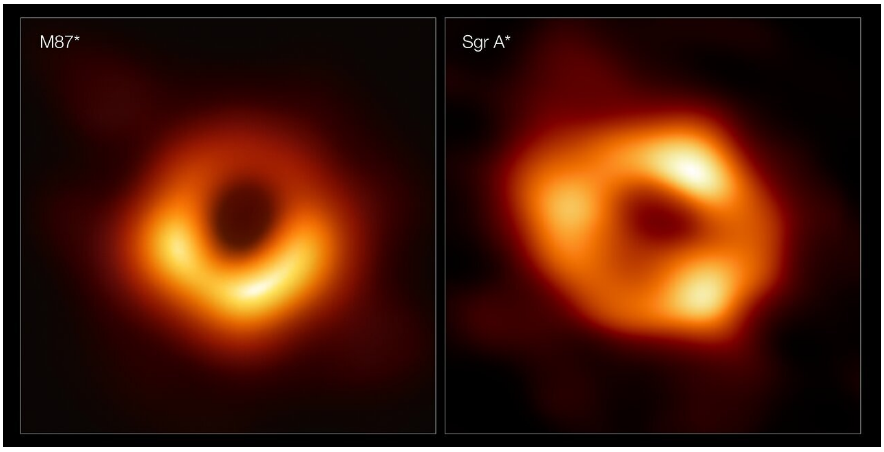

Figure 2.2: Image of the black hole at the center of the galaxy M87 (left) and the Milky Way (right). Credit: EHT Collaboration.

al., 2003; Spera, Mapelli, and Bressan, 2015). At higher metallicities, black holes above this gap are not expected to exist due to enhanced mass loss, while in some scenarios very massive stars may undergo pair-instability or runaway thermonuclear explosions, leaving no compact remnant (Heger and Woosley, 2002; Heger, Fryer, et al., 2003). The lower end of the stellar-mass black hole range is set by the maximum mass of neutron stars, which is estimated to lie around $2-3\,\mathrm{M}_\odot$, although uncertainties in the equation of state of dense matter may allow for a mass gap between neutron stars and black holes (Farr et al., 2011). Overall, stellar-mass black holes are expected to span masses from a few solar masses up to $\sim 100\,\mathrm{M}_\odot$ (Cosimo Bambi, 2018a). Observationally, stellar-mass black holes are typically found in XRBs, where dynamical mass measurements indicate masses in the range $3-20\,\mathrm{M}_\odot$ (Casares and Jonker, 2014). Gravitational-wave detections have extended this range by revealing the existence of heavier stellar-mass black holes, such as those involved in the GW150914 event (B. P. Abbott, R. Abbott, T. D. Abbott, Abernathy, et al., 2016). Figure 2.1 shows the number of black holes and neutron stars discovered via gravitational waves since the first detection, compared with those discovered using electromagnetic observations over the past 60 years. The plot demonstrates the power of gravitational-wave astronomy for observing compact objects and reveals a region of the universe that has, until now, been largely inaccessible to electromagnetic telescopes.

Supermassive black holes (SMBHs) are believed to exist at the centers of most galaxies, with masses ranging from $\sim 10^5-10^{10}\,\mathrm{M}_\odot$. The most robust evidence for SMBHs comes from detailed observations of stellar motions and gas dynamics in galactic nuclei, particularly in the Milky Way and NGC 4258, which allow precise estimates of the central mass. Although present in most galaxies, the formation channels of SMBHs remain poorly understood, particularly how they can grow to such large masses within a relatively short time (Volonteri, 2010). Proposed scenarios include rapid growth through super-Eddington accretion, direct collapse of massive primordial gas clouds, and hierarchical growth via mergers of smaller black holes (Madau, Haardt, and Dotti, 2014; Volonteri, 2010). The Milky Way itself hosts a central SMBH, Sagittarius A*. A major milestone was achieved in 2019 with the release of the first image of a SMBH in M87 (Event Horizon Telescope Collaboration, Akiyama, Alberdi, Alef, Asada, et al., 2019), followed in 2022 by the first image of the SMBH at the center of the Milky Way (Event Horizon Telescope Collaboration, Akiyama, Alberdi, Alef, Algaba, et al., 2022); both are shown in Fig. 2.2.

Intermediate-mass black holes (IMBHs) are hypothesized to bridge the mass gap between stellar-mass and supermassive black holes, with expected masses of roughly $10^2 - 10^4\,\mathrm{M}_\odot$ (Coleman Miller and E. J. M. Colbert, 2004). Despite extensive searches, their existence has not yet been confirmed through direct dynamical measurements, and their interpretation remains debated. Observational hints come primarily from ultra-luminous X-ray sources (Edward J. M. Colbert and Mushotzky, 1999) and detections of QPOs (Pasham, Strohmayer, and Mushotzky, 2014), which may indicate compact objects more massive than typical stellar remnants. However, the former can often be explained by extreme accretion onto stellar-mass black holes or neutron stars, while QPOs remain poorly understood, leaving the existence of IMBHs uncertain and an open problem in astrophysics.

2.1.3 X-Ray Binaries

This thesis focuses on stellar-mass accreting black holes in XRBs. These systems are commonly divided into low-mass and high-mass systems (LMXBs and HMXBs), where this classification refers to the mass of the donor star rather than to the compact object. In LMXBs, the companion is typically a low-mass star with mass $M \leq 3\,\mathrm{M}_\odot$, whereas HMXBs host a massive companion with $M \geq 10\,\mathrm{M}_\odot$. From an observational perspective, black hole XRBs can also be distinguished as either *transient* or *persistent* X-ray sources (Cosimo Bambi, 2018a). This behaviour is closely related to the dominant accretion mechanism. Accretion in X-ray binaries generally proceeds via two main channels: Roche-lobe overflow and stellar-wind capture (Tauris and van den Heuvel, 2006). In LMXBs, the donor star commonly fills its Roche lobe, leading to mass transfer through the inner Lagrange point and the formation of an accretion disc around the black hole. In contrast, HMXBs are typically powered by the capture of the strong stellar wind emitted by the massive companion star. A schematic view of a LMXB undergoing Roche-lobe overflow is shown in Fig. 2.3. The companion star transfers mass onto the compact object, forming an accretion disc whose innermost regions emit strongly in the X-rays.

LMXBs are most often observed as transient systems, characterised by episodic outbursts separated by long intervals of quiescence. During these outbursts, which can last from days to several months, the X-ray luminosity increases dramatically as the accretion rate through the disc rises, while quiescent phases may persist for years or even decades. HMXBs, on the other hand, are usually persistent

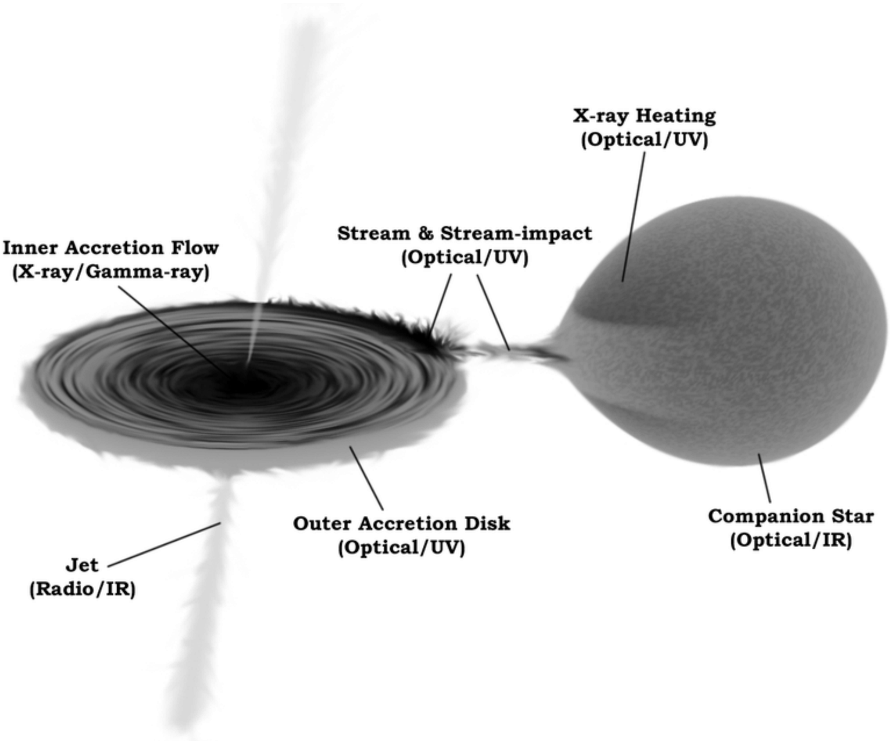

Figure 2.3: Geometry of a Roche lobe overflow LMXB. The color scale is inverted with the brightest areas appearing darkest. Reproduced from Hynes, 2014. © Cambridge University Press 2014.

X-ray emitters, as the mass supply from the companion's stellar wind is comparatively steady, resulting in continuous accretion onto the black hole (Cosimo Bambi, 2018a).

Such systems are often accompanied by the presence of a hot, optically thick electron cloud called corona surrounding the inner regions of the accretion disc. The relative strength of the thermal component from the disk and the non-thermal (power-law, as we will see in next sections), as well as the X-ray variability, define the spectral states of an XRB. During an outburst, it is natural that the spectrum of the source changes (Cosimo Bambi, 2018a).

A useful tool to track the evolution of spectral states during an outburst, and to study transient XRBs, is the hardness-intensity diagram (HID) (T. Belloni et al., 2005), shown in Fig. 2.4. In this diagram, the y-axis represents the X-ray luminosity, while the x-axis measures the spectral hardness, defined as the ratio of the source luminosity in a hard X-ray band to that in a soft X-ray band (e.g., $6-10$ keV / $2-6$ keV, though other choices are also common). Black hole XRBs typically follow a well-defined evolutionary track in the HID during an outburst. This track is illustrated in Fig. 2.4, commonly referred to as the "q" diagram because of the characteristic shape traced by the source in the HID. In general, when the thermal emission from the accretion disk dominates over the higher-energy emission associated with the corona, the source is observed in the soft state. Conversely, when the non-thermal, high-energy component is stronger, the source is in the hard state. The intensity of the thermal component is mainly determined by the mass accretion rate and the position of the inner edge of the disk, while the the contributions of the non-thermal component depend on the properties of the corona.

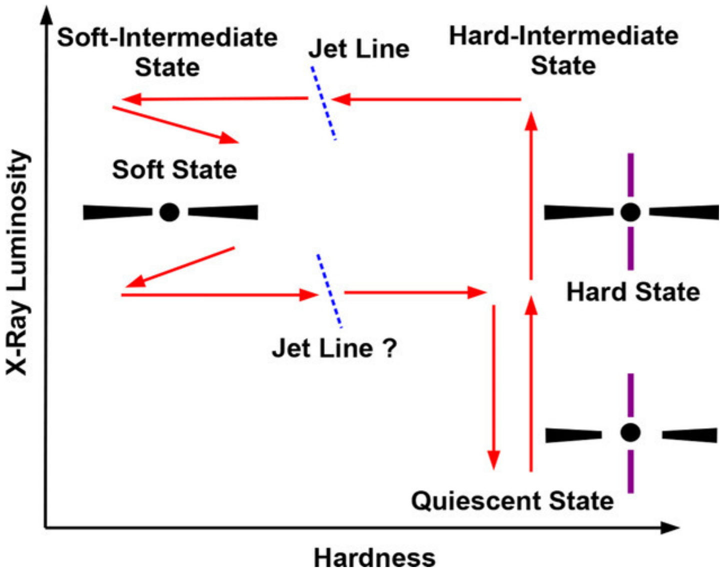

Figure 2.4: Spectral evolution of XRBs during an outburst in the HID. The source is initially in a quiescent state. At the beginning of the outburst, the source enters the hard state, then moves to some intermediate states, to the soft state, and eventually returns to a quiescent state. From Cosimo Bambi, 2018a. © 2018 John Wiley & Sons, Inc. Reproduced with permission.

Getting into the details of this "spectral journey", the source starts in a *quiescent state*, characterized by very low accretion rate, low luminosity, a hard spectrum, and a truncated accretion disk. As the mass accretion rate increases, the system enters the *hard state*. The luminosity rises, the spectrum is dominated by non-thermal emission, and steady compact jets are commonly observed, although the mechanism behind them is still unknown. As the luminosity increases, the inner disk gradually moves inward. With further spectral softening, the source passes through the hard- and soft-intermediate states, marked by a decreasing contribution from the corona and an increasing thermal disk component. The jet line present in Fig. 2.4 is associated with the observation of transient highly relativistic jets, although it is not well inderstood yet. The soft state is reached when the thermal emission from the disk dominates the spectrum and the disk extends down to the radius of the ISCO, assuming a luminosity of $5 - 30\%$ of the Eddington limit[1] (Jeffrey E. McClintock et al., 2006). Jets are quenched, while winds or outflows may also be present. As the accretion rate declines, the source returns to quiescence. While the general counter-clockwise evolution in the HID is common, significant differences can occur between sources and between different outbursts of the same system. In the case of persistent X-ray sources, there are no outbursts, but we can still use the HID (see, e.g., Done, Gierliński, and Kubota, 2007; Remillard and Jeffrey E. McClintock, 2006; Cosimo Bambi, 2018a).

2.2 The Kerr Spacetime

The motion of particles around black holes is determined by the spacetime metric and, in the specific case considered here, by the Kerr metric. In this section, we introduce the Kerr spacetime, focusing on circular orbits in the equatorial plane. This choice is motivated by the Novikov-Thorne model, where the gas particles in the disk move on nearly geodesic circular orbits in the equatorial plane, while the inner edge of the disk is located at the radius of the *innermost stable circular orbit*, value which is determined by the spin of the black hole. This section is adapted from Section 10.3 of Cosimo Bambi, 2018b and Section 12.7 of Stuart L. Shapiro and Teukolsky, 1983.

2.2.1 Metric & Horizon(s)

The Kerr solution is the unique solution of the Einstein equations describing a four-dimensional, asymptotically flat, stationary, axisymmetric, vacuum black hole. In Boyer-Lindquist coordinates, the line element is (Kerr, 1963; Boyer and Richard W. Lindquist, 1967):

$$\begin{aligned} ds^2 = &-\left(1-\frac{2Mr}{\Sigma}\right)dt^2 - \frac{4aMr\sin^2\theta}{\Sigma}dtd\phi \\ &+\frac{\Sigma}{\Delta}dr^2 + \Sigma d\theta^2 + \left(r^2+a^2+\frac{2a^2Mr\sin^2\theta}{\Sigma}\right)\sin^2\theta d\phi^2, \end{aligned} \tag{2.6}$$

where:

[1] An important concept in the context of XRBs is the *Eddington luminosity*, or *Eddington limit* (L_{Edd}). This corresponds to the luminosity at which the outward force due to radiation pressure on the emitting material balances the inward gravitational force of the compact object. The Eddington luminosity represents the maximum luminosity that can be sustained by a generic object, and is not specific to black holes. Assuming the emitting medium is a fully ionized gas of protons and electrons, the Eddington luminosity of an object of mass M is:

$$L_{\mathrm{Edd}} = \frac{4\pi G M m_p c}{\sigma_{\mathrm{th}}} = 1.26\cdot 10^{38}\left(\frac{M}{\mathrm{M}_\odot}\right)\ \mathrm{ergs/s}, \tag{2.5}$$

where G is the gravitational constant, m_p is the mass of the proton and σ_{th} is the Thomson cross section.

$$\Sigma = r^2 + a^2 \cos^2\theta, \tag{2.7}$$
$$\Delta = r^2 - 2Mr + a^2, \tag{2.8}$$
$$a = J/M, \tag{2.9}$$

in which J is the spin angular momentum of the black hole. In the forthcoming analysis, we will often make use of the dimensionless spin parameter:

$$a_* = \frac{a}{M} = \frac{J}{M^2}. \tag{2.10}$$

In contrast to the Schwarzschild metric, which is static, the Kerr metric is stationary and axisymmetric about the polar axis. This means it possesses two Killing vectors: a timelike one associated with time translations and a spacelike one associated with rotations around the axis of symmetry. In other words, the metric coefficients are independent of t and ϕ.

The event horizons of a Kerr black hole occur where the metric function Δ vanishes, yielding two solutions::

$$r_\pm = M \pm \sqrt{M^2 - a^2}. \tag{2.11}$$

The outer horizon, r_+, corresponds to the actual black hole horizon, while the inner horizon, r_-, lies deeper inside the black hole. For horizons to exist, the spin parameter must satisfy $|a| \leq M$. Otherwise, the solution describes a *naked singularity*. A major open question in General Relativity is *Penrose's Cosmic Censorship Conjecture*, which posits that gravitational collapse from physically reasonable initial conditions cannot produce naked singularities (Roger Penrose, 1969).

2.2.2 Orbits in the Equatorial Plane

The Lagrangian of a test-particle, or in our case, a parcel of gas, is given by:

$$\mathcal{L} = \frac{1}{2} g_{\mu\nu} \dot{x}^\mu \dot{x}^\nu, \tag{2.12}$$

where the dot indicates the derivative in respect to the proper time τ.

The line element of a generic stationary and axisymmetric spacetime can always be written in the following form:

$$ds^2 = g_{tt}dt^2 + 2g_{t\phi}dtd\phi + g_{rr}dr^2 + g_{\theta\theta}d\theta^2 + g_{\phi\phi}d\phi^2, \tag{2.13}$$

where the metric coefficients are independent of t and ϕ.

Since the metric is independent of the coordinates t and ϕ, we have two constants of motion, namely the specific energy at infinity E and the axial component of the specific angular momentum at infinity L_z:

$$\frac{d}{d\tau}\frac{\partial\mathcal{L}}{\partial\dot{t}} - \frac{\partial\mathcal{L}}{\partial t} = 0 \Rightarrow p_t \equiv \frac{\partial\mathcal{L}}{\partial\dot{t}} = g_{tt}\dot{t} + g_{t\phi}\dot{\phi} = -E, \tag{2.14}$$

$$\frac{d}{d\tau}\frac{\partial\mathcal{L}}{\partial\dot{\phi}} - \frac{\partial\mathcal{L}}{\partial \phi} = 0 \Rightarrow p_\phi \equiv \frac{\partial\mathcal{L}}{\partial\dot{\phi}} = g_{t\phi}\dot{t} + g_{\phi\phi}\dot{\phi} = L_z. \tag{2.15}$$

Combining Eqs. 2.14 and 2.15 we can obtain the temporal and azimuthal components of the 4-velocity of the test particle:

$$\dot{t} = \frac{Eg_{\phi\phi} + L_z g_{t\phi}}{g_{t\phi}^2 - g_{tt}g_{\phi\phi}}, \tag{2.16}$$

$$\dot{\phi} = -\frac{Eg_{t\phi} + L_z g_{tt}}{g_{t\phi}^2 - g_{tt}g_{\phi\phi}}. \tag{2.17}$$

The normalization condition of the four-velocity reads (using the convention of a metric with signature $(-+++)$):

$$g_{\mu\nu}\dot{x}^\mu\dot{x}^\nu = -1, \tag{2.18}$$

and therefore using Eqs. 2.14 and 2.15, we can rewrite Eq. 2.18 in the convenient form:

$$g_{rr}\dot{r}^2 + g_{\theta\theta}\dot{\theta}^2 = V_{\text{eff}}(r,\theta), \tag{2.19}$$

where V_{eff} is the effective potential:

$$V_{\text{eff}} = \frac{E^2 g_{\phi\phi} + 2EL_z g_{t\phi} + L_z^2 g_{tt}}{g_{t\phi}^2 - g_{tt}g_{\phi\phi}}. \tag{2.20}$$

Circular equatorial orbits are characterized by the zeros and extrema of the effective potential. In particular, the conditions $\dot{r} = \dot{\theta} = 0$ imply that:

$$V_{\text{eff}} = 0, \tag{2.21}$$

while the vanishing of the second derivatives, $\ddot{r} = \ddot{\theta} = 0$, requires:

$$\partial_r V_{\text{eff}} = 0 \quad \text{and} \quad \partial_\theta V_{\text{eff}} = 0. \tag{2.22}$$

These relations allow us to determine the specific energy E and the axial component of the specific angular momentum L_z of a test particle moving on equatorial circular orbits. Nevertheless, a more efficient approach is adopted below.

We start from the Langrangian (Eq. 2.12) and we apply the the Euler-Lagrange equations:

$$\frac{d}{d\tau}\left(\frac{\partial\mathcal{L}}{\partial\dot{x}^\mu}\right) - \frac{\partial\mathcal{L}}{\partial x^\mu} = 0 \Rightarrow \frac{d}{d\tau}(g_{\mu\nu}\dot{x}^\nu) - \frac{1}{2}(\partial_\mu g_{\nu\rho})\dot{x}^\nu\dot{x}^\rho = 0. \tag{2.23}$$

Rearranging the terms, we express the geodesic equations in the form:

$$\frac{d}{d\tau}(g_{\mu\nu}\dot{x}^\nu) = \frac{1}{2}(\partial_\mu g_{\nu\rho})\dot{x}^\nu\dot{x}^\rho. \tag{2.24}$$

In the case of equatorial circular orbits ($\dot{r} = \dot{\theta} = \ddot{r} = 0$) the radial component of Eq. 2.24 reduces to:

$$(\partial_r g_{tt})\,\dot{t}^2 + 2(\partial_r g_{t\phi})\,\dot{t}\dot{\phi} + (\partial_r g_{\phi\phi})\,\dot{\phi}^2 = 0. \tag{2.25}$$

Solving Eq. 2.25 with respect to $\Omega = \dot{\phi}/\dot{t}$, we obtain a relation for the angular velocity (Ω):

$$\Omega_\pm = \frac{-\partial_r g_{t\phi} \pm \sqrt{(\partial_r g_{t\phi})^2 - (\partial_r g_{tt})(\partial_r g_{\phi\phi})}}{\partial_r g_{\phi\phi}}, \tag{2.26}$$

where the $(+)$ and $(-)$ signs correspond to corotating and counterrotating orbits, respectively.

Using Eq. 2.18 with $\dot{r} = \dot{\theta} = 0$, we can write:

$$\dot{t} = \frac{1}{\sqrt{-g_{tt} - 2\Omega g_{t\phi} - \Omega^2 g_{\phi\phi}}}. \tag{2.27}$$

Substituting Eq. 2.27 into Eqs. 2.14 and 2.15, we obtain:

$$E = -(g_{tt} + \Omega g_{t\phi})\dot{t} = -\frac{g_{tt} + \Omega g_{t\phi}}{\sqrt{-g_{tt} - 2\Omega g_{t\phi} - \Omega^2 g_{\phi\phi}}}, \tag{2.28}$$

$$L_z = (g_{t\phi} + \Omega g_{\phi\phi})\dot{t} = -\frac{g_{t\phi} + \Omega g_{\phi\phi}}{\sqrt{-g_{tt} - 2\Omega g_{t\phi} - \Omega^2 g_{\phi\phi}}}. \tag{2.29}$$

Employing the metric coefficients of the Kerr solution in Boyer-Lindquist coordinates, Eqs. 2.28, 2.29 and 2.26 become, respectively (James M. Bardeen, Press, and Teukolsky, 1972):

$$E = \frac{r^{3/2} - 2Mr^{1/2} \pm aM^{1/2}}{r^{3/4}\sqrt{r^{3/2} - 3Mr^{1/2} \pm 2aM^{1/2}}}, \tag{2.30}$$

$$L_z = \pm\frac{M^{1/2}(r^2 \mp 2aM^{1/2}r^{1/2} + a^2)}{r^{3/4}\sqrt{r^{3/2} - 3Mr^{1/2} \pm 2aM^{1/2}}}, \tag{2.31}$$

$$\Omega_\pm = \pm\frac{M^{1/2}}{r^{3/2} \pm aM^{1/2}}, \tag{2.32}$$

where the the upper sign refers to corotating orbits and the lower sign to counterrotating ones.

In the study of accretion disks and the emitted spectra of black hole X-ray binaries, a precise definition of the inner edge of the disk is essential. In the Novikov-Thorne disk model, the inner edge of the disk is located at the ISCO, also known as the *marginally stable orbit*. Within the Kerr metric, equatorial circular orbits are found to be vertically stable[2]. As a result, the location of the ISCO is fixed entirely by the radial stability condition:

$$\partial_r^2 V_{\text{eff}} = 0 \quad\Rightarrow\quad r = R_{\text{isco}}. \tag{2.33}$$

[2]The equatorial plane is always a minimum of the potential in the vertical direction ($\partial_\theta^2 V_{\text{eff}} > 0$ for every circular equatorial orbit in Kerr).

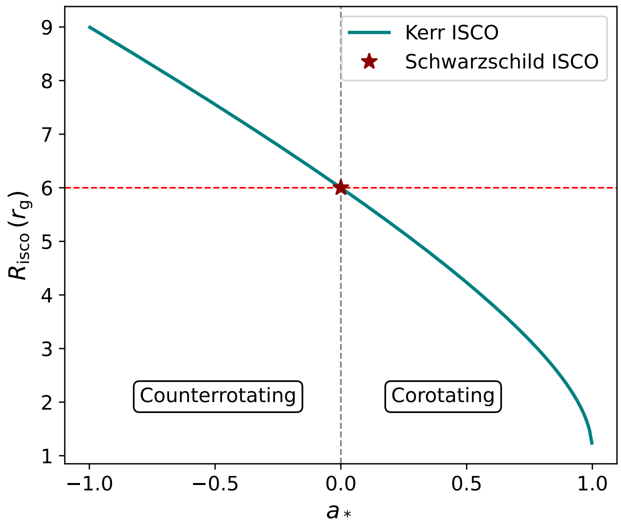

Figure 2.5: ISCO radius as a function of the dimensionless black hole spin parameter. Positive spin corresponds to corotating orbits, while negative spin corresponds to counterrotating orbits. The star indicates the Schwarzschild ISCO at $6\,r_{\rm g}$.

In Boyer-Lindquist coordinates, one obtains (James M. Bardeen, Press, and Teukolsky, 1972):

$$\begin{aligned} R_{\rm isco} &= 3M + Z_2 \mp \sqrt{(3M - Z_1)(3M + Z_1 + 2Z_2)}, \\ Z_1 &= M + (M^2 - a^2)^{1/3}\left[(M+a)^{1/3} + (M-a)^{1/3}\right], \\ Z_2 &= \sqrt{3a^2 + Z_1^2}. \end{aligned} \tag{2.34}$$

Figure 2.5 shows the dependence of the ISCO on the black hole spin. For a maximally spinning black hole ($a_* = 1$), the ISCO for a prograde orbit lies at $r_{\rm g}$ ($r_{\rm g} = GM/c^2$), while for a retrograde orbit it is at $9\,r_{\rm g}$. In the case of a non-spinning black hole ($a_* = 0$, Schwarzschild) $R_{\rm isco} = 6\,r_{\rm g}$. It is worth noting that the concept of the ISCO does not exist in Newtonian mechanics. By writing the equations of motion in terms of an effective potential, we see that close to the black hole the potential is dominated by an additional attractive term, absent in Newtonian theory, which is responsible for the existence of the innermost stable circular orbit.

Finally, an alternative way to determine the ISCO is by locating the minimum of the orbital energy, see Eq. 2.28. After some algebra, one finds that, in the corotating case, this condition is equivalent to the minimum of the axial component of the angular momentum (considering the corotating case). This behavior is illustrated in Fig. 2.6, where both the energy and the angular momentum are plotted as functions of the orbital radius. The minima of these curves identify

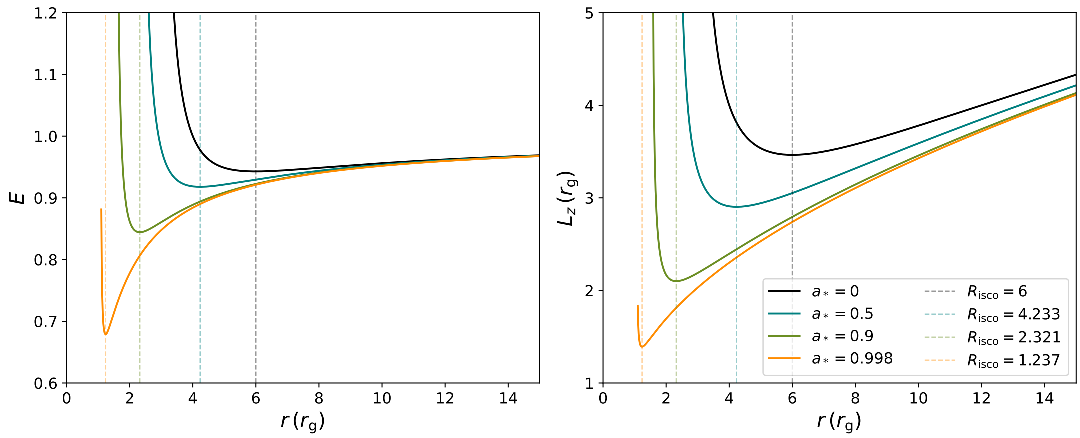

Figure 2.6: Energy (left panel) and axial angular momentum (right panel) for equatorial circular orbits around a Kerr black hole as functions of the orbital radius, and for different spin values. The minima of the curves identify the ISCO radius, indicated by the dotted vertical lines.

the ISCO, which is marked by the dotted vertical lines. We note that all curves are plotted up to the *photon orbit*, defined as the radius at which the denominator of Eqs. 2.28 and 2.29 vanishes. This feature is clearly visible in the plot only for the orange curve.

2.2.3 Frame Dragging

Let us now examine Eq. 2.15, which describes the specific angular momentum of a test particle as measured at infinity, L_z. Even if we set $L_z = 0$, the test particle can still possess a non-zero angular velocity, in the case of a non-vanishing off-diagonal metric component $g_{t\phi}$:

$$\Omega = \frac{\dot{\phi}}{\dot{t}} = -\frac{g_{t\phi}}{g_{\phi\phi}}. \tag{2.35}$$

In other words, a particle with zero angular momentum at infinity can nevertheless acquire a non-zero angular velocity. This occurs because a spinning compact object induces a deformation of the surrounding spacetime, effectively “dragging” the particle along with it. Such an effect is entirely absent in Newtonian gravity, where the gravitational influence of a body depends solely on its mass, and its angular momentum produces no additional effects. In General Relativity, however, the angular momentum of a massive body directly affects the spacetime geometry.

This phenomenon, known as *frame dragging*, refers to the ability of a spinning massive object to “drag” the surrounding spacetime along with it. An intuitive analogy is a vortex in water: objects placed near the vortex are carried along by the swirling flow, much like test particles are compelled to rotate

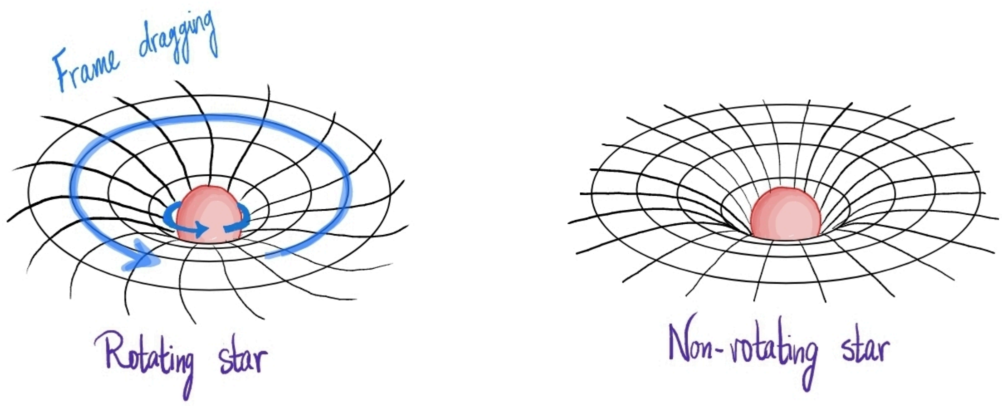

Figure 2.7: Illustration of the space-time geometry around a non-rotating star (right) and around a rotating star (left). In the case of the rotating star, there is the phenomenon of frame dragging. Figure reproduced from Zilberman, 2025, © 2026 Little, Big Science.

around a spinning compact object due to the curvature of spacetime. Figure 2.7 provides a schematic illustration of the spacetime surrounding a non-rotating (Schwarzschild) and a rotating (Kerr) black hole, with the effect of frame dragging clearly visible in the latter.

A generalization of the *static observers* of the Schwarzschild metric to the case of rotating black holes is provided by the *stationary* ones, who remain at fixed r and θ while rotating with a constant angular velocity Ω. Using Eq. 2.18 for a stationary observer, we obtain:

$$\dot{t}^2(g_{\phi\phi}\Omega^2 + 2g_{t\phi}\Omega + g_{tt}) = -1, \tag{2.36}$$

where Ω is given by Eq. 2.35. For this equation to be consistent, the quantity inside the parentheses must be negative. Since $g_{\phi\phi} > 0$, this condition is satisfied only if Ω lies between the roots of the quadratic equation obtained by setting the parentheses to zero. Explicitly, we have:

$$\Omega_{\text{min}} < \Omega < \Omega_{\text{max}}, \tag{2.37}$$

with:

$$\Omega^{\text{max}}_{\text{min}} = \frac{-g_{t\phi} \pm \sqrt{g_{t\phi}^2 - g_{tt}g_{\phi\phi}}}{g_{\phi\phi}}. \tag{2.38}$$

The lower bound Ω_{min} becomes zero when $g_{tt} = 0$, which corresponds to:

$$r^2 - 2Mr + a^2\cos^2\theta = 0 \Rightarrow R_+ = M + \sqrt{M^2 - a^2\cos^2\theta}. \tag{2.39}$$

Observers located between r_+ and R_+ must have $\Omega > 0$, implying that no static observers can exist in the region $r_+ < r < R_+$. This area is called the *ergoregion*, where the effect of frame dragging is particularly strong. The surface $r = R_+$

defines the *static limit*, which is also called *boundary of the ergosphere*. The ergosphere is shown in Fig. 2.8, which illustrates the evolution of the event horizon and ergosphere for increasing black hole spin.

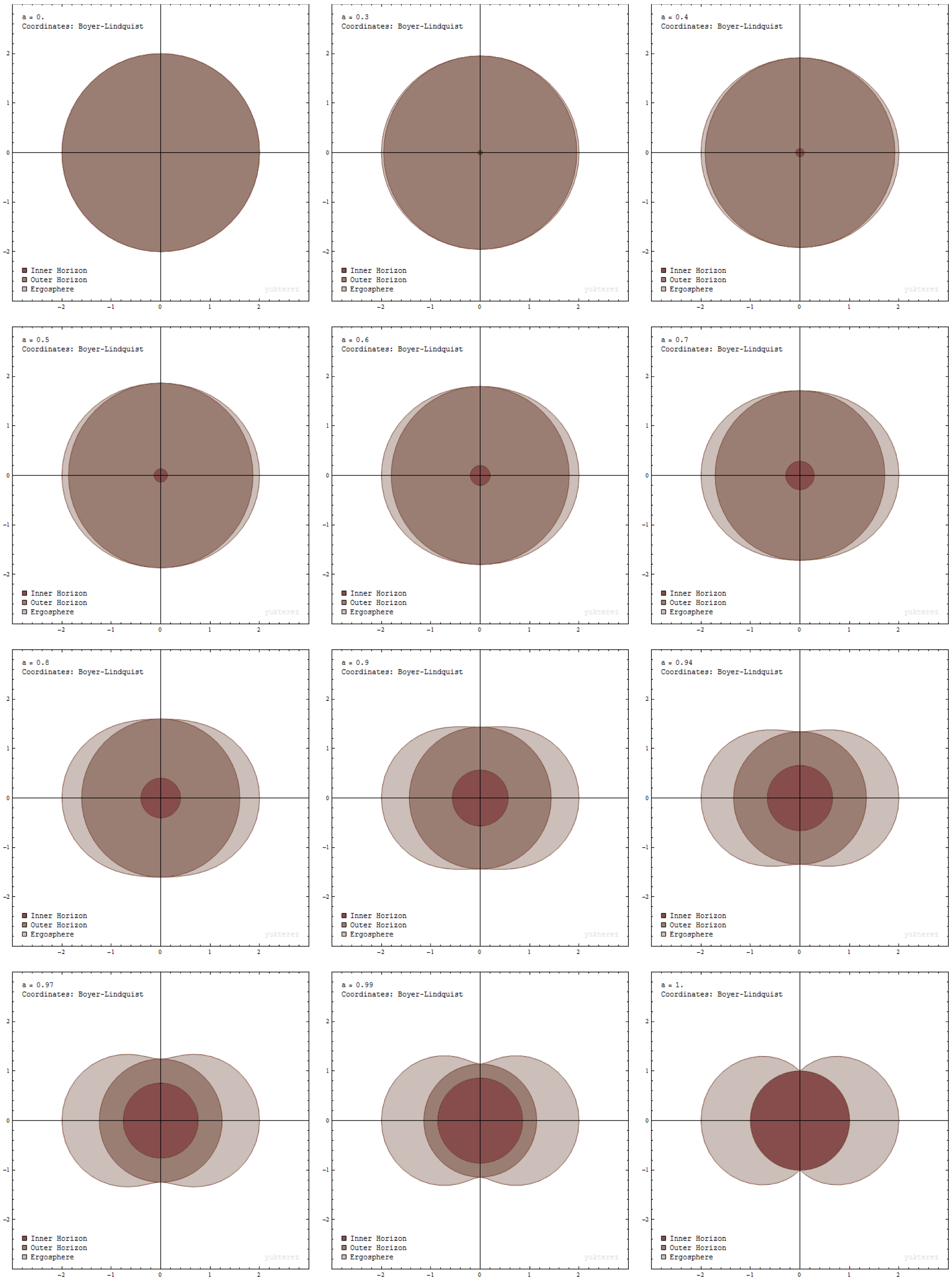

Figure 2.8: Sequence illustrating the deformation of the event horizon and ergosphere for increasing black hole spin. Images are extracted and adapted from the animation by Yukterez, 2016, licensed under CC BY-SA 4.0.

2.3 Novikov-Thorne Accretion Disk

The standard framework for describing a geometrically thin and optically thick accretion disk is the Novikov-Thorne model (Novikov and K. S. Thorne, 1973; Page and K. S. Thorne, 1974), which represents the relativistic generalization of the Shakura-Sunyaev disk (Shakura and Sunyaev, 1973). This model is formulated in a generic stationary, axisymmetric, and asymptotically flat spacetime, such as the Kerr spacetime. While the calculation of relativistic reflection spectra only requires knowledge of particle motion in the equatorial plane of a thin disk, these assumptions are not sufficient for computing relativistic thermal spectra (C. Bambi, 2024). In that case, a disk model capable of predicting the radial temperature profile of the disk is required. This is precisely what the Novikov-Thorne model provides. In this section, we briefly discuss the assumptions of the model and its fundamental equations. For a comprehensive treatment, we refer the reader to Novikov and K. S. Thorne, 1973; Page and K. S. Thorne, 1974. This chapter is adapted from Sections 6.1 and 6.4 of C. Bambi, 2017 and Section VIII of C. Bambi, 2024.

2.3.1 Assumptions

The Novikov-Thorne model describes geometrically thin, optically thick accretion disks around black holes, in which viscous stresses, magnetic turbulence, and radiative processes collectively drive the outward transport of angular momentum and energy (Page and K. S. Thorne, 1974). The model is based on the following assumptions:

- The spacetime is stationary, axisymmetric, asymptotically flat, reflection-symmetric with respect to the equatorial plane, and the disk's influence on the spacetime metric is negligible.
- The disk lies in the equatorial plane, perpendicular to the black hole spin, with gas particles moving on nearly geodesic circular orbits, allowing the application of the formalism introduced in Section 2.2.
- The inner edge of the disk is located at the ISCO radius.
- The disk is geometrically thin, $h/r \ll 1$, and optically thick, $h \gg \lambda$, where h is the scale height at radius r and λ is the photon mean free path.
- Magnetic fields are neglected, and only photons with $\lambda \ll M$ carry away energy and angular momentum from the disk surface.
- Energy and angular momentum are radiated from the disk surface, while radial heat transport and returning radiation are ignored.
- A time-averaged treatment is employed, assuming the timescale is short enough to approximate the spacetime as stationary, yet long enough to neglect possible inhomogeneities in the accreting matter.

Some of the assumptions in the thin-disk model are very strict, while others can be relaxed. For instance, the requirement of a geometrically thin disk cannot be easily relaxed, since the structure of a thick disk is fundamentally different. Nevertheless, applying the thin-disk approximation to systems near the Eddington accretion limit can introduce significant systematic uncertainties, as the disk becomes progressively thicker and the thin-disk description no longer holds (Riaz, Ayzenberg, et al., 2020a; Riaz, Ayzenberg, et al., 2020b). The assumption that the inner edge of the disk coincides with the ISCO radius can, in principle, be relaxed to allow larger inner radii. However, this has a substantial impact on spin measurements via reflection spectroscopy, because the exact location of the inner edge strongly affects the reflection features in the spectrum.

Assuming an infinitesimally thin, Keplerian disk often provides accurate results for rapidly rotating sources, as demonstrated by general relativistic magnetohydrodynamic (GRMHD) simulations (S. Shashank et al., 2022) and by analyses of specific sources using models that allow deviations from Keplerian motion or finite disk thickness (A. B. Abdikamalov et al., 2020; Tripathi, B. Zhou, et al., 2020; Tripathi, A. B. Abdikamalov, et al., 2021; J. Jiang et al., 2022). For a comprehensive discussion on the validity of these assumptions, we refer to C. Bambi, 2017, Section 6.1.1.

2.3.2 Formulation

The strength of the Novikov-Thorne model lies in its ability to determine the time-averaged[3] radial structure of an accretion disk using only fundamental conservation laws, without relying on detailed properties of the accreting fluid. Starting from the conservation of rest mass, expressed as:

$$\nabla_\mu(\rho u^\mu) = 0, \tag{2.41}$$

where ρ is the time-averaged rest-mass density and u^μ is the time-averaged four-velocity of the fluid, we integrate this equation over over the 3-volume of the disk extending from radius r to $r + \Delta r$ and over a time interval Δt. Applying the Gauss's theorem, we obtain that the time-averaged mass accretion rate is independent of the radius r:

$$\dot{M} = -2\pi\sqrt{-\mathcal{G}}\tilde{\Sigma}u^r = \text{constant}, \tag{2.42}$$

where $\mathcal{G} = -a^2 g_{rr} g_{\phi\phi}$ is the determinant of the metric in the equatorial plane and $a^2 = g_{t\phi}^2/(g_{\phi\phi} - g_{tt})$ is the lapse function, while:

$$\tilde{\Sigma} = \int_{-h}^{h} \rho \, dz, \tag{2.43}$$

[3]The time averaged value of any real quantity $A(t, r, \theta, \phi)$ is defined as:

$$\langle A \rangle = \frac{1}{2\pi\Delta t}\int_0^{\Delta t}\int_0^{2\pi} A(t, r, \theta, \phi)\, dt d\phi. \tag{2.40}$$

In the following analysis the notation $\langle A \rangle$ will be omitted for simplicity.

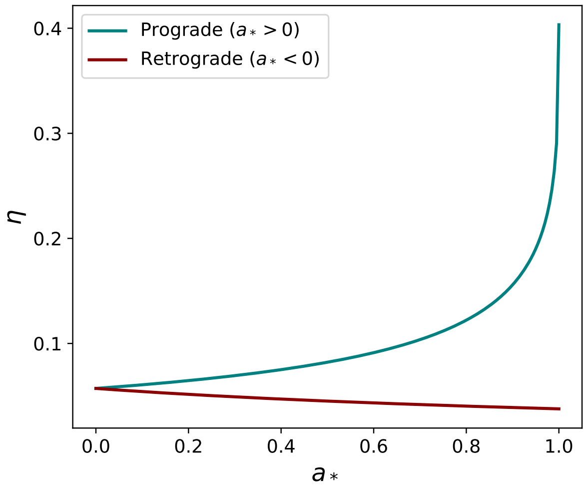

Figure 2.9: Radiative efficiency as a function of the spin parameter in the Kerr metric. The blue and red curves correspond to corotating and counterotating orbits, respectively.

represents the time-averaged surface density of the disk, where z is the vertical axis of the cylindrical coordinates.

Similarly, by using the conservation laws of energy and angular momentum:

$$\nabla_\mu T^{t\mu} = 0, \quad \nabla_\mu T^{\phi\mu} = 0, \tag{2.44}$$

one can derive the time-averaged energy flux emitted from the disk surface $\mathcal{F}(r)$ and the time-averaged torque $W^r_\phi(r)$:

$$\mathcal{F}(r) = \frac{\dot{M}}{4\pi M^2} F(r), \tag{2.45}$$

$$W^r_\phi(r) = \frac{\dot{M}}{2\pi M^2} \frac{\Omega L_z - E}{\partial_r \Omega} F(r), \tag{2.46}$$

where E, L_z and Ω are the conserved specific energy (Eq. 2.28), specific angular momentum along the rotation axis (Eq. 2.29), and angular velocity of equatorial circular orbits (Eq. 2.26), respectively. The dimensionless function $F(r)$ is:

$$F(r) = -\frac{\partial_r \Omega}{(E - \Omega L_z)^2} \frac{M^2}{\sqrt{-\mathcal{G}}} \int_{r_{\rm in}}^{r} (E - \Omega L_z)(\partial_r L_z)\, dr, \tag{2.47}$$

where $r_{\rm in}$ is the inner radius of the disk, typically set at ISCO. For disks truncated at larger radii, a different $r_{\rm in}$ can be used without changing the form of $F(r)$.

At leading order, the total power generated by accretion, $L_{\rm acc}$, is converted into radiation and the kinetic energy of jets or outflows. The total efficiency is therefore:

$$\eta_{\rm tot} = \frac{L_{\rm acc}}{\dot{M}} = \eta_r + \eta_k, \tag{2.48}$$

where η_r is the radiative efficiency, measurable from the bolometric luminosity $L_{\text{bol}} = \eta_r \dot{M}$ and η_k is the fraction of gravitational energy converted to kinetic energy of jets and outflows, usually neglected in the Novikov-Thorne framework.

In the Novikov-Thorne model, gas particles gradually spiral inward toward the black hole, and upon reaching the ISCO, they rapidly plunge into the black hole without emitting further radiation. Assuming that η_k is negligible, the efficiency reduces to[4]:

$$\eta = \eta_r = 1 - E\,(R_{\text{isco}}), \tag{2.49}$$

where $E\,(R_{\text{isco}})$ is the specific energy of a test-particle at the ISCO radius. The dependence of the efficiency on the spin parameter is shown in Fig. 2.9. For a Schwarzschild black hole, $\eta \approx 0.057$, while for a maximally rotating prograde and retrograde black hole, $\eta \approx 0.423$ and $\eta \approx 0.038$, respectively.

Assuming that the disk material is in local thermal equilibrium, one can introduce an effective temperature T_{eff} at each radial coordinate by requiring that the energy flux $\mathcal{F}$ in Eq. 2.45 corresponds to the thermal power radiated from the disk surface. Under this assumption, the Stefan-Boltzmann law yields:

$$\mathcal{F} = \sigma_{\text{SB}} T_{\text{eff}}^4, \tag{2.50}$$

where σ_{SB} denotes the Stefan-Boltzmann constant. A useful order-of-magnitude estimate for the effective temperature is:

$$T_{\text{eff}} \sim \left(\frac{10\,\mathrm{M}_\odot}{M}\right)^{1/4} \text{ keV}, \tag{2.51}$$

which implies that the characteristic temperature in the inner regions of an accretion disk around a $10\,\mathrm{M}_\odot$ black hole is of order ~ 1 keV, whereas for a supermassive black hole with mass $M \sim 10^9\,\mathrm{M}_\odot$ it is of order ~ 10 eV. Figure 2.10 illustrates the impact of the spin parameter on the radial profile of the effective temperature in Novikov-Thorne disks around a $10\,\mathrm{M}_\odot$ Kerr black hole with $\dot{M} = 10^{18}$ g/s. Far from the black hole, the profile is Newtonian ($T_{\text{eff}} \propto R^{-3/4}$).

In accretion disks around stellar-mass black holes, the effective temperature in the innermost regions is sufficiently high that non-thermal effects, most notably electron scattering in the disk atmosphere, become important and cannot be neglected. As a result, the emergent spectrum deviates from that of a perfect blackbody. These deviations are commonly accounted for by introducing a *color factor* (or *hardening factor*) f_{col}, which relates the color temperature to the effective temperature according to:

$$T_{\text{col}} = f_{\text{col}} T_{\text{eff}}. \tag{2.52}$$

[4]The radiative efficiency measures the fraction of rest-mass energy of the infalling gas that is radiated away before the gas plunges into the black hole:

$$\eta = \frac{\text{energy radiated}}{\text{rest mass energy}} = \frac{E\,(\infty) - E\,(R_{\text{isco}})}{E\,(\infty)} = \frac{1 - E\,(R_{\text{isco}})}{1} = 1 - E\,(R_{\text{isco}}),$$

where the energy at infinity is normalized to unity, corresponding to the rest-mass energy.

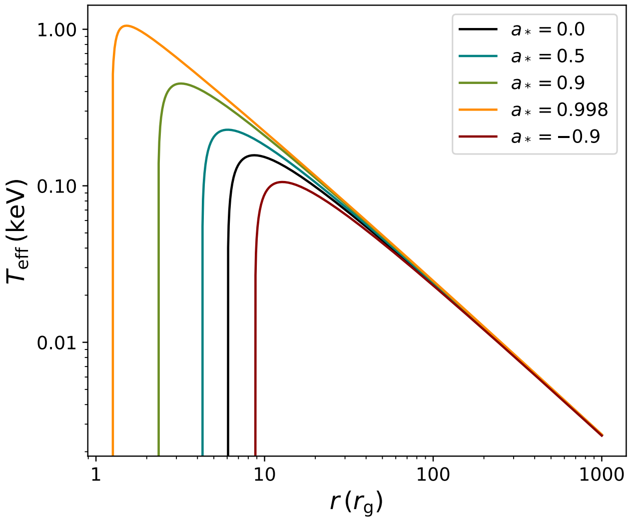

Figure 2.10: Effective temperature radial profile of a Novikov-Thorne disk around a $10\,\mathrm{M}_\odot$ Kerr Black hole with $\dot{M} = 10^{18}\,\mathrm{g/s}$, for different values of the spin parameter.

The specific intensity of the radiation in the rest-frame of the material in the disk is:

$$I = \frac{2h\nu_{\rm e}^3}{c^2}\frac{1}{f_{\rm col}^4}\frac{\Upsilon}{e^{\frac{h\nu_{\rm e}}{k_{\rm B}T_{\rm col}}} - 1}, \tag{2.53}$$

where $\nu_{\rm e}$ is the emitted photon frequency, h is Planck's constant, c is the speed of light, and $k_{\rm B}$ is the Boltzmann constant. The factor $\Upsilon = \Upsilon(\theta_{\rm e})$ accounts for the angular dependence of the emission.

In the Kerr spacetime, the local thermal emission at each radius is fully specified by the black hole mass M, the mass accretion rate $\dot{M}$, the dimensionless spin parameter a_*, the color correction factor $f_{\rm col}$ (typically in the range $1.5-1.9$), and the angular emissivity function Υ. The two most commonly adopted prescriptions are $\Upsilon = 1$, corresponding to isotropic emission, and $\Upsilon = 0.5 + 0.75\cos\theta_{\rm e}$, which describes limb-darkened emission.

2.3.3 The Thorne Limit

Accretion from a geometrically thin disk provides an efficient channel for spinning up a black hole. But, is there an upper spin limit from this process? To address this question, we consider a parcel of gas that gradually spirals toward the black hole down to the ISCO radius, after which it plunges rapidly into the black hole without further radiative losses. Under these assumptions, the accretion of matter leads to infinitesimal changes in the black hole mass and angular momentum according to:

$$M \to M + \delta M, \quad J \to J + \delta J, \tag{2.54}$$

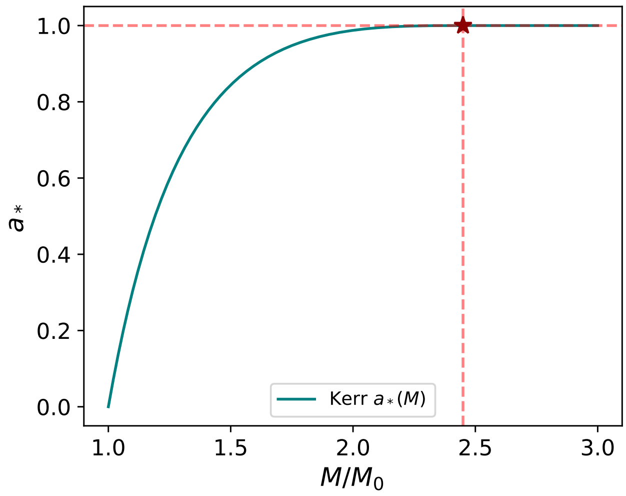

Figure 2.11: Spin evolution of a Kerr black hole according to Eq. 2.56, neglecting the effect of radiation captured by the black hole. The black hole is initially non-rotating with mass M_0. The star marks the equilibrium point, where $M = \sqrt{6}\, M_0$ and $a_* = 1$.

where δM and δJ are the mass and angular momentum carried by the gas, respectively, defined as:

$$\delta M = E(R_{\rm isco})\, \delta m, \quad \delta J = L(R_{\rm isco})\, \delta m, \tag{2.55}$$

where δm is the gas rest mass. The evolution of the dimensionless spin parameter can be expressed in terms of the logarithmic change in the black hole mass:

$$\frac{da_*}{d\ln M} = \frac{1}{M}\frac{L(R_{\rm isco})}{E(R_{\rm isco})} - 2a_*. \tag{2.56}$$

Naturally, Spin-up (spin-down) occurs when the right-hand side of this equation is positive (negative), while an equilibrium configuration is reached when it vanishes. For a Kerr black hole, the resulting evolution equation can be solved analytically, yielding an explicit expression for the spin as a function of mass (James M. Bardeen, 1970):

$$a_* = \begin{cases} \sqrt{\frac{2}{3}\frac{M_0}{M}} \left(4 - \sqrt{18\dfrac{M_0^2}{M^2} - 2}\right) & \text{if } M \leq \sqrt{6}\, M_0, \\ 1 & \text{if } M > \sqrt{6}\, M_0, \end{cases} \tag{2.57}$$

assuming an initially non-rotating black hole with mass M_0. Notably, the equilibrium value of the spin reaches the extremal value $a_* = 1$, which is achieved once the black hole mass has increased by a factor of $\sqrt{6} \approx 2.4$. The spin evolution is illustrated in Fig 2.11.

In reality, however, not all radiation emitted by the accretion disk escapes to infinity. A fraction of the emitted photons is captured by the black hole, thereby contributing additional energy and angular momentum to it. This effect can be incorporated by adding a correction term to Eq. 2.49:

$$\eta = 1 - E\left(R_{\text{isco}}\right) - \zeta_{\text{E}}, \tag{2.58}$$

where ζ_{E} accounts for the radiation captured by the black hole. An analogous term ζ_{L} accounts for the angular momentum. A detailed discussion and explicit expressions for these quantities can be found in Kip S. Thorne, 1974.

When these corrections are included, Eqs. 2.55 and 2.56 take the form:

$$\delta M = \left[E(R_{\text{isco}}) + \zeta_{\text{E}}\right] \delta m, \quad \delta J = \left[L(R_{\text{isco}}) + \zeta_{\text{L}}\right] \delta m, \tag{2.59}$$

$$\frac{da_*}{d\ln M} = \frac{1}{M} \frac{L(R_{\text{isco}}) + \zeta_{\text{L}}}{E(R_{\text{isco}}) + \zeta_{\text{E}}} - 2a_*. \tag{2.60}$$

Solving Eq. 2.60 in the Kerr spacetime yields an equilibrium spin known as the *Thorne limit* (Kip S. Thorne, 1974):

$$a_*^{\text{Th}} \approx 0.998, \tag{2.61}$$

which implies that it is impossible to spin a black hole up to the extremal limit. This behavior closely parallels the third law of thermodynamics (J. M. Bardeen, Carter, and Hawking, 1973), which states that absolute zero temperature cannot be reached through a finite sequence of physical processes. Similarly, the third law of black hole mechanics forbids reaching $a_* = 1$ via accretion of a finite amount of mass.

2.4 X-Ray Reflection Spectroscopy

Reflection spectroscopy is the study of reflection spectra from XRBs to probe the inner part of accretion disks, test General Relativity and most importantly, measure black hole spins. The observed spectrum of black hole XRBs typically consists of three primary components: (i) a thermal component originating from a geometrically thin, optically thick accretion disk (Shakura and Sunyaev, 1973; Page and K. S. Thorne, 1974); (ii) a Comptonized component produced by a hot corona that inverse-Compton scatters soft disk photons (K. S. Thorne and Price, 1975; S. L. Shapiro, Lightman, and Eardley, 1976); and (iii) a reflection component resulting from the illumination of the disk by the corona (George and Fabian, 1991). The disk is thought to be cold as it can efficiently emit radiation and its thermal spectrum peaks in the soft X-rays (~ 1 keV). The system is modelled via the so-called disk-corona model, presented in Fig. 2.12.

The corona is a region of hot plasma ($\sim 10 - 100$ keV) located near the black hole. Its emitted spectrum is commonly modeled empirically as a power-law with an exponential high-energy cutoff, E_{cut}:

$$\frac{dN_{\text{c}}}{dt_{\text{c}}\, dE_{\text{c}}} = K E_{\text{c}}^{-\Gamma} e^{-\frac{E_{\text{c}}}{E_{\text{cut}}}}, \tag{2.62}$$

where Γ is the photon index (often close to 2), K is a normalization constant, and the subscript c indicates that the quantities are measured in the rest frame of the corona (T. Mirzaev, C. Bambi, et al., 2024).

The precise geometry of the corona remains uncertain. Figure 2.13 illustrates several commonly discussed coronal configurations. In the lamppost model, the corona is treated as a point-like source located along the black hole spin axis; for instance, the base of a jet may act as a lamppost corona (Markoff, Nowak, and Jörn Wilms, 2005). In the sandwich model, the corona corresponds to a hot atmosphere extending above and below the accretion disk. In spherical and toroidal models, the corona is the hot material in the plunging region, between the inner edge of the accretion disk and the black hole. The coronal geometry may evolve over time, on timescales as short as hours or days in the case of XRBs, and multiple coronal components may coexist simultaneously (C. Bambi, 2024). For a broader discussion and comparative evaluation of different coronal geometries, see e.g., C. Bambi, 2017 and S. Li et al., 2025.

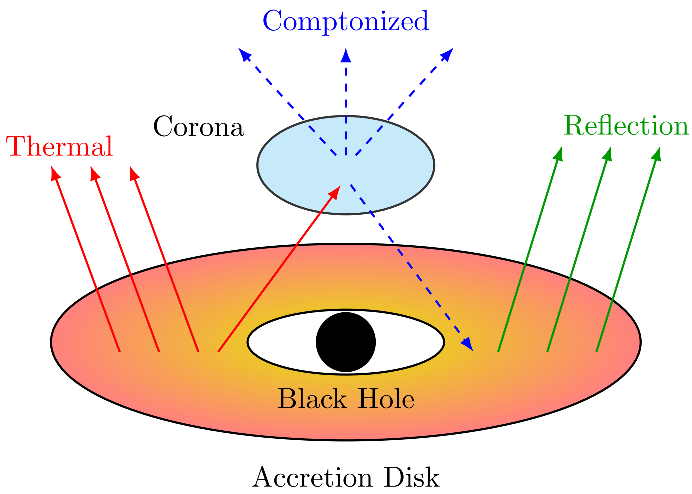

Figure 2.12: Schematic illustration of a black hole-disk-corona model including thermal, Compton, and reflection components. The color gradient in the disk indicates that the temperature increases towards the black hole.

In the rest frame of the accretion disk material, the reflected X-ray spectrum typically features narrow fluorescent emission lines at lower energies and a pronounced Compton hump peaking between 20 and 40 keV (Ross and Fabian, 2005; J. Garcia and T. R. Kallman, 2010). The most notable spectral line is generally the iron Kα complex, which appears at 6.4 keV for neutral or weakly ionized iron, and shifts up to 6.97 keV for fully ionized, hydrogen-like iron[5]. However,

[5] As the ionization increases, reduced electron shielding results in a higher effective nuclear charge, shifting the line energy upwards.

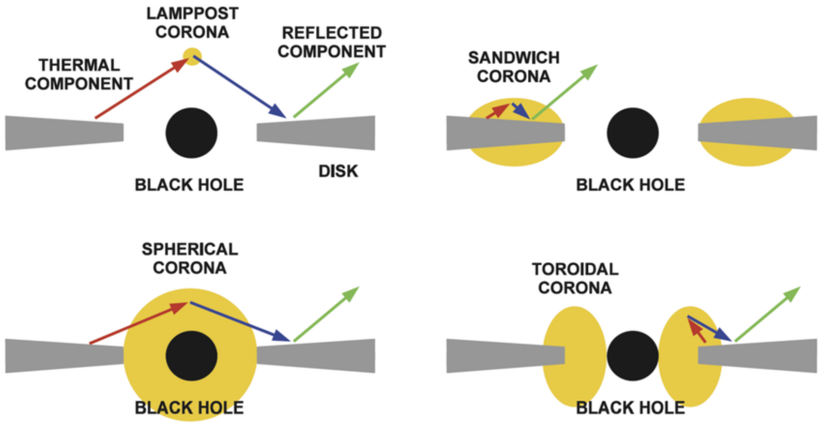

Figure 2.13: Examples of possible corona geometries: lamppost geometry (top left panel), sandwich geometry (top right panel), spherical geometry (bottom left panel), and toroidal geometry (bottom right panel). Figure reproduced from Cosimo Bambi, 2017. © 2017 Springer Nature Singapore Pte Ltd. Reproduced with permission.

when observed from a distant point, the disk's entire reflection spectrum appears smeared due to relativistic effects (Fabian, Rees, et al., 1989; Laor, 1991; Fabian, Iwasawa, et al., 2000; T. Dauser, J. Wilms, et al., 2010).

In this section, we explain the reflection process, the resulting reflection spectra including relativistic effects, discuss returning radiation, and review the current state of research and limitations in X-ray reflection spectroscopy. This section is adapted from Section 1.4 of Liu, 2024.

2.4.1 Local Reflection

The local reflection spectrum of the disk is shaped by *fluorescence emission* and *Compton scattering*. Focusing on fluorescence, when an incident photon has energy greater than the binding energy of the K-shell, it can be absorbed, creating a vacancy. An electron from a higher shell, typically the L-shell, can then transition to fill this vacancy, emitting a photon with energy equal to the difference between the two shells. In some cases, instead of emitting a photon, the energy can be transferred to another electron, which is then ejected (*Auger effect*).

This process occurs for all elements in the disk, but the probability of fluorescence increases rapidly with atomic number ($\sim Z^4$ for neutral matter). Given iron's large atomic number and relatively high abundance, it dominates the emission lines. In particular, photons with energy above 7.1 keV can be absorbed by neutral iron (Fe I), removing a K-shell electron and producing a photoelectric absorption edge in the reflection spectrum. Subsequently, an electron from the L-shell ($n = 2$) can transition to the K-shell, emitting an X-ray photon with energy of 6.4 keV, known as the iron Kα line. Iron lines are especially important because there are few other lines around 6.4 keV, whereas the spectrum below 4

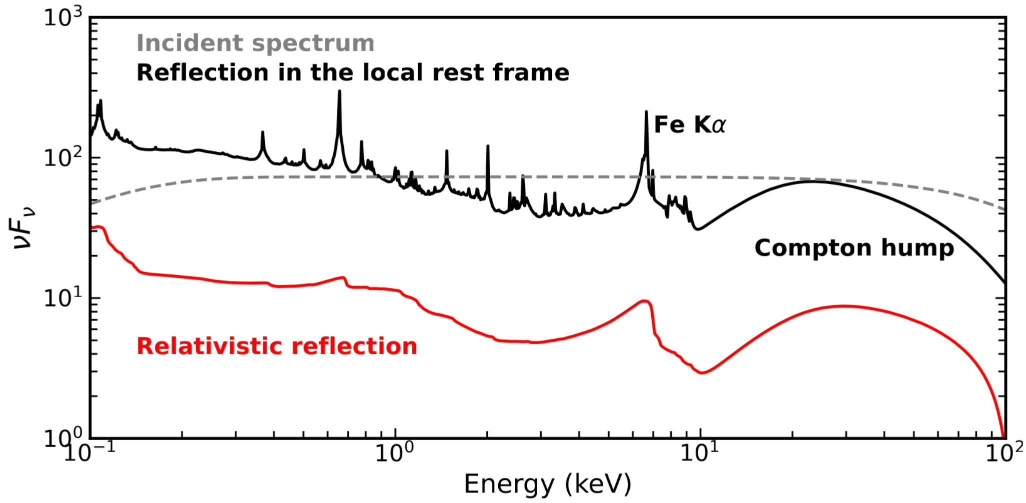

Figure 2.14: Rest-frame reflection (black) and relativistic reflection (red) spectra for an accretion disk extending to the ISCO. The red spectrum is shifted vertically for visual clarity. The incident spectrum is a Comptonized continuum. From Liu, 2024. Reproduced with permission of the author.

keV contains many overlapping lines.

The degree of ionization of the disk material significantly affects both the shape and the energy of the emission lines. The *ionization parameter* (ξ) at each radius r is defined as:

$$\xi(r) = \frac{4\pi\Phi_{\rm X}(r)}{n_{\rm e}(r)}, \tag{2.63}$$

where $\Phi_{\rm X}(r)$ is the incident flux and $n_{\rm e}(r)$ is the electron number density[6]. When the disk is weekly or mildly ionized, the spectrum shows a complex of emission lines at energies between 6.4 to 6.7 keV, corresponding to the iron Kα line. At low electron densities, the disk surface becomes highly ionized, reducing photoelectric opacity and suppressing fluorescent line production. As a result, characteristic reflection features, particularly the Fe Kα line, are weakened and the spectrum becomes dominated by a smooth Compton-scattered continuum. Typical range of values for the electron density is 10^{15} to $10^{22}\,\mathrm{cm^{-3}}$, while for the ionization parameter ranges from ~ 100 for weekly ionized to $\sim 5000\,\mathrm{erg\,cm\,s^{-1}}$ for a completely ionized disk.

At higher photon energies, electron scattering becomes the dominant interac-

[6] As a first approximation, we can consider the electron density along the disk constant; however, it is natural to consider an electron density profile, such as the one of the Shakura-Sunyaev model (Shakura and Sunyaev, 1973):

$$n_{\rm e}(r) \propto \frac{r^{3/2}}{\left[1-(r_{\rm in}/r)^{1/2}\right]^2}, \tag{2.64}$$

where the minimum value of the density is e.g. $10^{15}\,\mathrm{cm^{-3}}$.

tion. This transition occurs around 12 keV, where the electron scattering cross-section equals the photoelectric absorption cross-section. Since the disk is relatively cold, high-energy photons that scatter off electrons lose energy through Compton down-scattering. The interplay of the iron K-edge absorption and Compton down-scattering of these photons produces the characteristic *Compton hump* in the spectrum, peaking around $20 - 30$ keV. The Compton hump and the Fe Kα emission line are visible in the black curve of Fig. 2.14, which shows a typical reflection spectrum in the rest frame of the disk material.

Finally, the *element abundances* in the accretion disk have a significant impact on the reflection spectrum, as they determine the probability of interactions between X-ray photons and the atoms or ions in the disk. Most reflection models assume solar abundances for all elements except iron. The disk's composition is largely set by the type of the donor star, which dictates the relative abundance of elements present. Variations in elemental abundances can therefore change the strength and shape of features such as the iron line and the Compton hump. The impact of the ionization parameter and the iron abundance on the local reflection spectra is shown in Fig. 2.15.

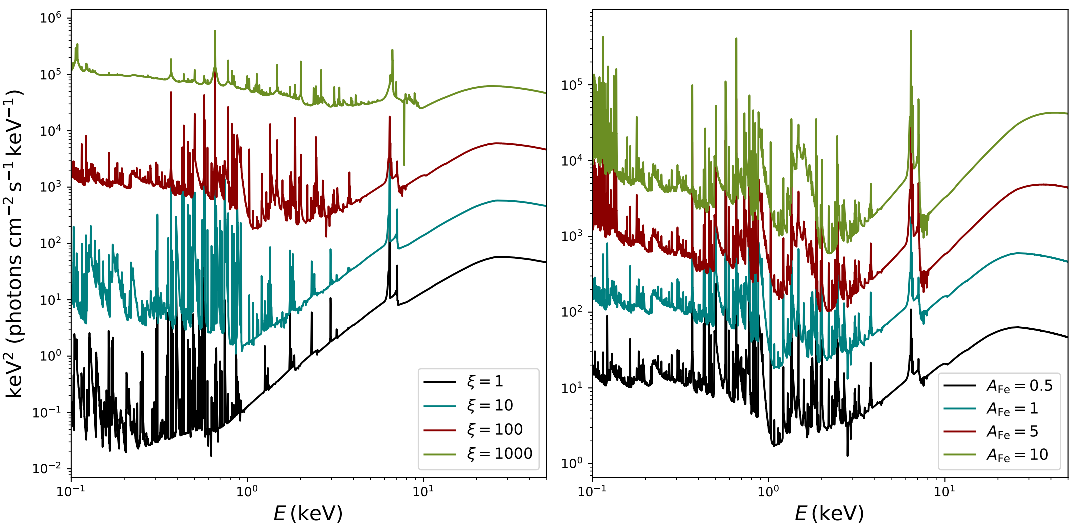

Figure 2.15: Impact of the ionization parameter (left panel) and iron abundance (right panel) on the local reflection spectra. In both panels, the spectra have been multiplied by factors of 1, 10, 100, and 1000 to avoid overlap. The spectra were produced with the `xillver` model, assuming $\Gamma = 2$ and $E_{\rm cut} = 300$ keV, with $A_{\rm Fe} = 1$ (solar value) in the left panel and $\xi = 100\,{\rm erg\,cm\,s^{-1}}$ in the right panel.

Computationally, non-relativistic reflection spectra are obtained using radiative transfer codes, the most widely used being `reflionx` (Ross and Fabian, 2005) and `xillver` (J. Garcia and T. R. Kallman, 2010; J. Garcia, T. Dauser, C. S. Reynolds, et al., 2013). The latter represents an updated reflection model that incorporates the `xstar` (T. Kallman and Bautista, 2001) photoionization code to compute the ionization equilibrium and the corresponding emissivities. Both models simulate the reflection spectrum produced by an optically thick slab illuminated by a primary X-ray source. For a detailed discussion and comparison between the two models, we refer to Section 3.3 of Temurbek Mirzaev, 2025.

2.4.2 Relativistic Reflection

The description of the emission presented so far refers to the rest frame of the accretion disk material. However, when observed by a distant observer, both individual emission lines and the overall reflection spectrum appear significantly broadened and distorted due to relativistic effects (Fabian, Rees, et al., 1989; Laor, 1991; Fabian, Iwasawa, et al., 2000; T. Dauser, J. Wilms, et al., 2010). In order to accurately infer the physical parameters of the system, reflection models must therefore incorporate the full set of relativistic corrections.

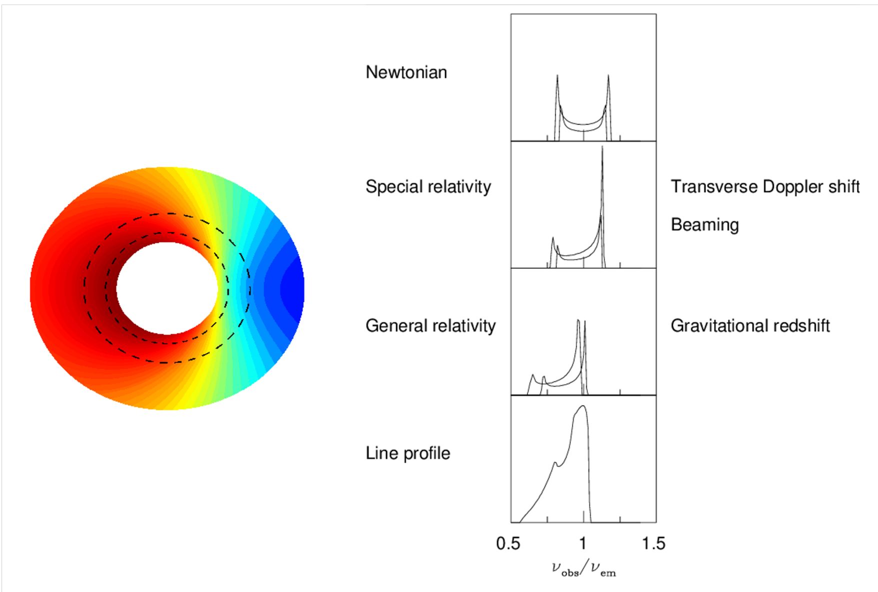

Figure 2.16: Emission line broadening due to relativistic effects. Figure reproduced from Fabian, Iwasawa, et al., 2000.

Figure 2.16 illustrates a rotating accretion disk and the resulting line broadening produced by different relativistic effects. In a purely Newtonian framework, the orbital motion of the disk material gives rise to a symmetric double-peaked line profile due to Doppler shifts. In the innermost regions of the disk, where the orbital velocities are highest, special relativistic effects become important and the blue-shifted peak is enhanced due to relativistic beaming. In addition, gravitational redshift becomes increasingly significant close to the black hole, producing an extended "red wing" in the line profile. The combined action of these effects, integrated over the entire disk, results in the characteristic relativistically broadened line profile shown in the bottom panel of Fig. 2.16.

The black hole spin, or equivalently the radius of the ISCO, has a strong impact on the relativistic reflection spectrum, since the inner edge of the accretion disk is assumed to be located at R_{isco}. As discussed in Section 2.2, in the Kerr metric there exists a one-to-one correspondence between the black hole spin and the ISCO radius. As shown in the left panel of Fig. 2.17, a smaller ISCO radius leads to stronger relativistic effects and causes the line profile to extend to lower energies. Reflection spectroscopy can therefore be used to estimate the black hole spin by modelling the degree of line broadening. The inclination angle of the disk also plays an important role in shaping the line profile: as the inclination increases (i.e., the disk is viewed more edge-on), the separation between the blue and red-shifted peaks increases and the line is "washed-out" due to stronger relativistic effects, as illustrated in the right panel of Fig. 2.17.

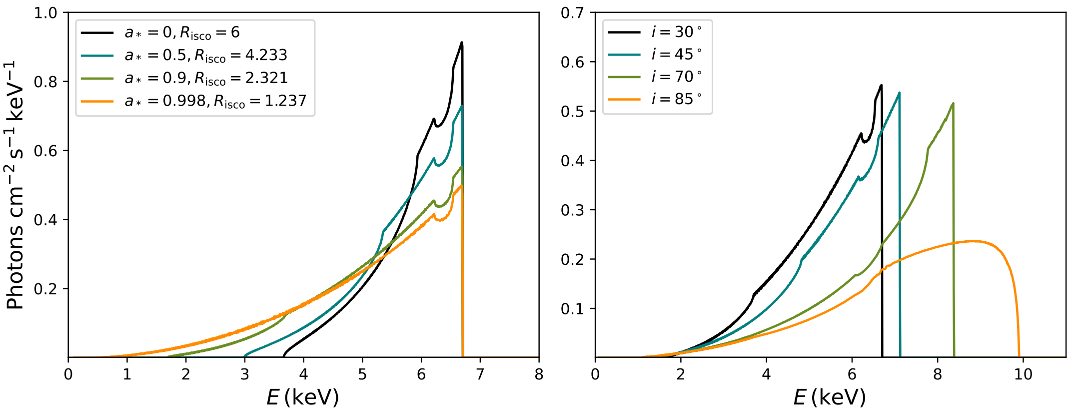

Figure 2.17: Dependence of the iron broad line profile from the spin (left panel) and the inclination angle (right panel). Both plots were created using the `relline` model ($E_{\text{line}} = 6.4\,\text{keV}$, emissivity index $q = 3$, $i = 30°$ (left) and $a_* = 0.9$ (right)).

Another key ingredient in determining the reflection spectrum is the *incident radiation* from the corona, as well as the *emissivity profile*, which describes the radial dependence of the incident coronal irradiation on the accretion disk. Both components are typically modelled empirically. The coronal emission is commonly described by a power-law spectrum with a high-energy cut-off, while the emissivity profile is often parameterized as a simple power-law ($\epsilon \propto r^{-q}$, where q is the emissivity index) or a broken power-law ($\epsilon \propto r^{-q_{\text{in}}}$ for $r < R_{\text{br}}$ and $\epsilon \propto r^{-q_{\text{out}}}$ for $r > R_{\text{br}}$, where R_{br} is the breaking radius). As mentioned earlier, the geometry of the corona remains uncertain, and in practice the emissivity profiles inferred from spectral fitting can be compared with theoretical predictions corresponding to different coronal geometries.

In reality, relativistic broadening affects not only individual emission lines but the entire local reflection spectrum. This is illustrated in Fig. 2.14, where the local (rest-frame) reflection spectrum is compared with the relativistically blurred one. In particular, the emission lines at lower X-ray energies are strongly smeared and cannot be individually resolved. As a result, the most prominent reflection features in observed spectra are the broad iron Kα line at $\sim 6-7$ keV and the Compton hump peaking at $\sim 20-30$ keV.

In practice, once the spectra in the rest frame of the disk in every radial bin is calculated (via e.g. `reflionx`), the relativistic spectra as seen by a distant observer is computed via *ray-tracing*. The observed spectral flux is given by (C. Bambi, 2024):

$$F_{\mathrm{o}}(E_{\mathrm{o}}) = \int_{source} I_{\mathrm{o}}(E_{\mathrm{o}}, X, Y)\, d\Omega = \frac{1}{D^2}\int_{source} g^3\, I_{\mathrm{e}}(E_{\mathrm{e}}, r_{\mathrm{e}}, \theta_e)\, dX\, dY, \tag{2.65}$$

where the subscripts o and e stand for observed and emitted respectively. D is the distance between the observer and the source, $g = E_{\mathrm{o}}/E_{\mathrm{e}}$ is the redshift factor and $I_{\mathrm{o}} = g^3 I_{\mathrm{e}}$, following from the Liouville's theorem (see R. W. Lindquist, 1966, for more details). X and Y are the the Cartesian coordinates in the plane of the distant observer and $d\Omega = dXdY/D^2$ the respective infinitesimal solid angle. Lastly, r_{e} denotes the radius at which the photon is emitted in the accretion disk, while θ_{e} represents the emission angle measured in the rest frame of the disk material. We consider a grid on the image plane of a distant observer and trace photons backward in time from each grid point. For every pixel, a photon is propagated from its detection point on the observer's image plane to its emission point on the accretion disk. When the photon intersects the disk at a radial coordinate r_e we compute the corresponding redshift factor g and the emission angle θ_e. Thus, for each pixel with Cartesian coordinates (X, Y) and area element $dXdY$ on the observer's image plane, the quantities g and the emitted specific intensity I_e are known, and we can therefore obtain the observed flux. For the calculation of the integral in Eq. 2.65, models often employ the so-called *transfer function* (C. T. Cunningham, 1975), which takes into account the photon relativistic effects (see, for instance, C. Bambi, 2017, Section 6.3). The details of the calculation of the relativistic reflection spectrum, can be found in Section VI of C. Bambi, 2024.

2.4.3 Current Models & Limitations

X-ray reflection spectroscopy has advanced significantly in recent years. The current state-of-the-art is represented by relativistic models such as `relxill`[7] (T. Dauser, J. Garcia, et al., 2013; J. Garcia, T. Dauser, Lohfink, et al., 2014), `reltrans`[8] (A. Ingram et al., 2019), `reflkerr` (Niedzwiecki and Zycki, 2008; Niedzwiecki, Szanecki, and Zdziarski, 2019), and `kyn`[9] (Dovciak, Karas, and Yaqoob, 2004), as well as radiative transfer models like `xillver` (J. Garcia, T. Dauser, C. S. Reynolds, et al., 2013) and `reflionx`[10] (Ross and Fabian, 2005), which compute the reflection spectra in the rest frame of the material of the disk. Despite these advances, current models still rely on a number of simplifications. Here, we highlight four issues (C. Bambi, 2024; Riaz, Ayzenberg, et al., 2020a):

[7] https://www.sternwarte.uni-erlangen.de/~dauser/research/relxill/
[8] https://github.com/reltrans/reltrans
[9] https://projects.asu.cas.cz/stronggravity/kyn
[10] https://github.com/honghui-liu/reflionx_tables

1. higher disk electron densities,
2. emission from the plunging region,
3. increased disk thickness,
4. returning radiation.

Concerning the first issue, non-relativistic reflection models often adopt electron densities lower than those expected in real astrophysical systems, particularly in XRBs in the soft state. Recent efforts have extended these calculations to higher densities, but they may still fall short of realistic values. Current models also typically assume a constant electron density along the vertical direction of the disk, and it remains unclear whether this is a reasonable approximation. For a further discussion, we refer to Ding et al., 2024 and Liu, Jiachen Jiang, et al., 2023.

The *plunging region* lies between the inner edge of the accretion disk and the black hole, where matter rapidly inspirals after leaving the disk. This region can be either optically thin or thick, depending on the local density. If optically thin, higher-order disk images may be visible, but their contribution to the relativistic reflection spectrum is negligible, particularly when the inner disk edge is very close to the black hole (M. Zhou et al., 2020). In optically thick cases, and in the absence of strong magnetic fields, the material is highly ionized and reflection occurs mainly via Compton scattering, producing a featureless spectrum that does not significantly affect measurements of key parameters such as spin or inclination (Cárdenas-Avendaño, M. Zhou, and Cosimo Bambi, 2020). The role of magnetic fields is less certain: weak fields reproduce the highly ionized, reflection-free case, while strong fields slow the plunging, increase density, reduce ionization, and can introduce reflection features, potentially causing a slowly rotating black hole to mimic a fast-rotating one in X-ray reflection spectroscopy.

Current relativistic reflection models typically assume that the accretion disk is infinitesimally thin, with its inner edge at the innermost stable circular orbit or at a larger radius. However, many sources, particularly supermassive black holes, accrete at rates near or above the Eddington limit, implying the presence of *geometrically thick disks*. In such cases, the disk geometry can deviate significantly from the standard thin-disk approximation. For example, the "Polish donut" model has been employed by Riaz, Ayzenberg, et al., 2020a; Riaz, Ayzenberg, et al., 2020b and showed that spin measurements are strongly affected by the accretion disk morphology. Consequently, current spin estimates for sources with high accretion rates should be interpreted with caution (see also Swarnim Shashank et al., 2026).

Returning radiation, as introduced in Chapter 1, is the radiation emitted by the accretion disk that, due to the strong gravitational bending near the black hole, returns to illuminate the disk itself. As emphasized throughout this work, returning radiation is the "main star of this thesis", and is therefore discussed independently in the next section.

2.4.4 Returning Radiation

The first calculations of returning radiation were performed by C. Cunningham, 1976 in the context of thermal disk spectra, while L.-X. Li et al., 2005 later showed that it can mimic the effect of a higher accretion rate. Although usually neglected in thermal spectral fitting, returning radiation has been shown to significantly influence polarization signatures (Schnittman and Krolik, 2009).

The role of returning radiation in reflection spectra was first examined in Dabrowski et al., 1997, who concluded it is negligible if the corona corotates with the disk. Niedzwiecki and Zycki, 2008 confirmed this but showed that the effect becomes important for a static corona close to the black hole. Subsequent studies in the lamppost geometry (Niedzwiecki, Zdziarski, and Szanecki, 2016; Niedzwiecki and Zdziarski, 2018) demonstrated that returning radiation can significantly alter the reflection spectrum under certain conditions. More recent work, employing a range of approximations, has further investigated this effect (Wilkins et al., 2020; T. Dauser, J. A. Garcia, et al., 2022; Riaz, Szanecki, et al., 2021; Riaz, T. Mirzaev, et al., 2023). These studies generally agree that returning radiation is especially relevant for rapidly spinning black holes ($a_* \geq 0.9$) with compact coronae illuminating the innermost disk (e.g., lamppost heights $h < 5\,r_g$).

Different approaches have been proposed to incorporate returning radiation in reflection modeling. For instance, T. Dauser, J. A. Garcia, et al., 2022 introduced a modified emissivity profile within `relxill`, though still assuming the illuminating flux follows a simple cutoff power-law in the disk rest frame. However, because the spectrum of returning radiation itself has the form of a reflection spectrum rather than a power-law, its effect cannot always be absorbed into emissivity modifications (T. Mirzaev, Riaz, et al., 2024). A model extensively used to describe thermal returning radiation is `relxillNS` (García, Thomas Dauser, et al., 2022). Although it was originally developed for neutron star reflection spectroscopy, it can mimic the effects of returning radiation as it illuminates the disk with a single-color temperature blackbody rather than a power-law continuum. For systems where the disk extends very close to the event horizon, returning radiation can substantially reshape the reflection spectrum. In such cases, computing the rest-frame reflection spectrum at each disk radius using the true incident spectrum, a mix of coronal power-law and returning radiation, becomes essential. Otherwise, spectral fits may fail, leading to significantly biased parameter estimates (T. Mirzaev, Riaz, et al., 2024).

Chapter 3

Model Development & Data Analysis

In the previous chapters, we introduced the theoretical background necessary to understand the physics of XRBs, accretion disks, and returning radiation. We now move on to the practical part of this work. Here, we show how a code that calculates relativistic reflection and blackbody spectra was adapted and integrated into the spectral fitting software XSPEC. This step is essential, since producing spectra alone does not allow direct comparison with observational data. By creating an XSPEC table model that includes returning radiation, we can fit real data and test theoretical predictions. In this chapter, we describe the generation of the XSPEC table model and assess its validity by fitting observational data from the XRB 4U 1630–47.

3.1 The `ziji` Code

The `ziji` code[1], presented in T. Mirzaev, C. Bambi, et al., 2024, computes local and relativistic reflection and blackbody spectra while self-consistently accounting for the effects of returning radiation[2]. In contrast to previous models (e.g., T. Dauser, J. A. Garcia, et al., 2022), the accretion disk is illuminated by the intrinsic spectrum rather than a power-law continuum. Figure 3.1 shows the fraction of photons that return to the disk, fall into the black hole or plunging region, or escape to infinity, and compares our results with those of T. Dauser, J. A. Garcia, et al., 2022, demonstrating good agreement between the two studies. Returning radiation is most important in the innermost regions of the disk, while at larger radii the majority of the photon flux escapes to infinity.

In this thesis, we model the reflection spectrum in the absence of coronal emission in order to isolate the contribution from returning radiation. The coronal component is disabled by setting its luminosity to zero, allowing us to isolate the

[1] https://github.com/ABHModels/ziji/

[2] A detailed description of the calculation of returning radiation in the `ziji` code is presented in Appendix B of T. Mirzaev, Riaz, et al., 2024.

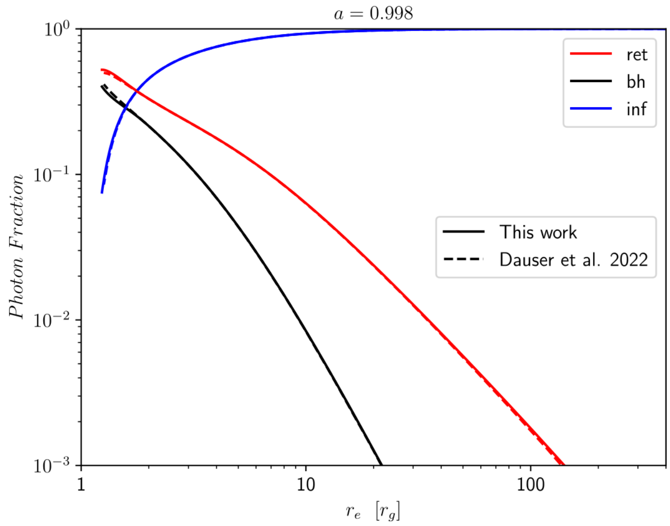

Figure 3.1: Fraction of photons returning to the accretion disk (returning radiation, red curves), falling onto the black hole or the plunging region (black curves), and escaping to infinity (blue curves) as a function of the radial coordinate of the emission point on the disk. The dotted curves correspond to the work of T. Dauser, J. A. Garcia, et al., 2022, while the solid ones to this work. Reproduced from T. Mirzaev, Riaz, et al., 2024.

effect of returning radiation on the reflection spectrum. While the code is capable of including a coronal component, in this thesis we deliberately neglect it.

The default spacetime metric in our model is the Kerr solution. However, the code does not rely on any specific equation or property of the Kerr metric, allowing us to adopt any stationary, axisymmetric, and asymptotically flat spacetime by simply modifying the metric coefficients (T. Mirzaev, C. Bambi, et al., 2024).

The accretion disk is described by the Novikov-Thorne disk (Page and K. S. Thorne, 1974; Novikov and K. S. Thorne, 1973), as described in Section 2.3. The ionization parameter of the disk is given by Eq. 2.63, assuming a constant electron density throughout the disk. The `ziji` code also treats iron abundance as a free parameter. Throughout all subsequent modeling, the iron abundance is fixed to the solar value ($A_{\rm Fe} = 1$). We note that we modified the `ziji` code to accept the mass accretion rate as an input parameter instead of the luminosity, as our primary interest lies in exploring variations in $\dot{M}_{\rm BH}$. A summary of the parameters included in the modified version of the code is presented in Table 3.1.

To compute the reflection spectrum in the rest frame of the disk, we use the `reflionx` code. We employ the `reflionx` code rather than the `reflionx` table, since the latter one assumes that the disk is illuminated by a power-law spectrum with a high-energy cutoff (T. Mirzaev, Riaz, et al., 2024). The radiation field incident on any point on the disk in our model includes only:

Parameter	Description
Black Hole mass ($M_{\rm BH}$)	Black hole mass in units of $\mathrm{M}_\odot$
Black hole spin (a_*)	Dimensionless black hole spin parameter
Disk electron density (n_e)	Electron density of the disk in units of electrons cm^{-3}; considered constant in this study
Inclination angle (i)	Disk inclination relative to the observer's line of sight (degrees)
Mass accretion rate ($\dot{M}_{\rm BH}$)	Mass accretion rate onto the black hole in g/s
Color factor ($f_{\rm col}$)	Default value 1.7
Iron abundance ($A_{\rm Fe}$)	Iron abundance in units of the Solar iron abundance (fixed at 1.0)
Disk emission (Υ)	Default function $\Upsilon = 1$ (isotropic emission)
Source distance (D)	Distance of the source (used for the normalization of the spectrum)
Inner edge of the disk ($r_{\rm in}$)	Radial coordinate of the inner edge of the disk (fixed at $R_{\rm isco}$)
Outer edge of the disk ($r_{\rm out}$)	Radial coordinate of the outer edge of the disk (fixed at $500\,r_{\rm g}$)

Table 3.1: Parameters of the modified `ziji` code applied in this study.

- returning thermal radiation (purple arrows in Fig. 3.2; 0th iteration),
- higher-order returning reflection radiation up to 3 iterations[3] (brown arrow in Fig. 3.2; 1st iteration).

After the calculation of the local reflection spectrum in every radial bin, the relativistic spectra as seen by a distant observer are computed via ray-tracing, using the `blackray`[4] code (Askar B. Abdikamalov et al., 2024). In contrast to other relativistic reflection models such as `relxill`, `ziji` does not rely on the transfer function approach; instead, it calculates the redshift factor directly via ray tracing (see Eq. 2.65). Moreover, the reflection spectra in our model does not explicitly depend on the local photon emission angle, instead, `ziji` uses an angle-averaged emission due to the `reflionx` code (see also Section 3.3.4). Finally, the resulting blackbody and reflection components are combined and stored in a FITS

[3]To avoid confusion, we note that in the papers where the `ziji` code was presented (T. Mirzaev, C. Bambi, et al., 2024; T. Mirzaev, Riaz, et al., 2024), up to 4 iterations were performed. The 0th iteration corresponds to the reflection component produced by the corona. In our case, there is no corona; therefore, we perform one fewer iteration (0–3). Physically, the procedure is identical.

[4]https://github.com/ABHModels/blackray

file compatible with XSPEC, generating a table model. A schematic overview of this pipeline is shown in Fig. 3.3.

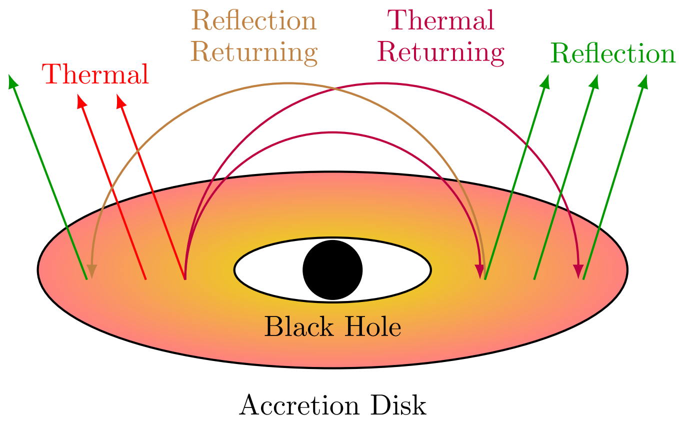

Figure 3.2: Schematic illustration of a black hole-disk model with reflection component from self-irradiation of the disk (thermal returning) and iterative reflection (reflection returning).

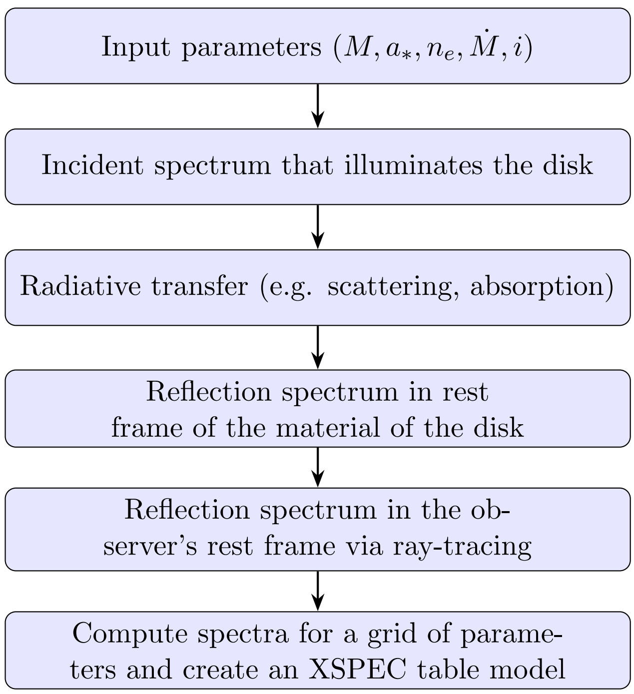

Figure 3.3: Schematic overview of the spectral calculation and XSPEC table-model generation pipeline.

3.2 Implementation in XSPEC

To construct the XSPEC table model, we compute blackbody and reflection spectra, using `ziji`, over a grid of parameters, as listed in Table 3.2. The spectra are combined into a custom additive XSPEC table model that includes 5 parameters:

1. electron density (n_{e}),
2. dimensionless spin parameter (a_*),
3. black hole mass (M_{BH}),
4. mass accretion rate ($\dot{M}_{\mathrm{BH}}$),
5. inclination angle (i).

The physical distance of the source is absorbed inside the normalization of the model, which is automatically introduced by XSPEC. The source distance can be inferred from the model normalization through the flux-luminosity relation:

$$F_{\mathrm{table}} = \frac{L}{4\pi D_{\mathrm{ref}}^2}, \quad F_{\mathrm{obs}} = \frac{L}{4\pi D_{\mathrm{source}}^2}, \tag{3.1}$$

and therefore:

$$F_{\mathrm{obs}} = \left(\frac{D_{\mathrm{ref}}}{D_{\mathrm{source}}}\right)^2 F_{\mathrm{table}}. \tag{3.2}$$

Here, F_{table} is the flux at the reference distance $D_{\mathrm{table}} = 10^6 r_{\mathrm{g}}$ used in the table model and F_{obs} is the flux at the true source distance D_{source}. Thus, the model's normalization plays the role of the geometric prefactor:

$$\mathcal{N} = (D_{\mathrm{ref}}/D_{\mathrm{source}})^2, \tag{3.3}$$

so that $F_{\mathrm{obs}} = \mathcal{N} F_{\mathrm{table}}$. We derive the following relation, which directly connects the model's normalization to the physical distance:

$$\mathcal{N} = 0.229 \cdot 10^{-20} \, \frac{M^2\,(\mathrm{M}_\odot)}{D^2\,(\mathrm{kpc})}. \tag{3.4}$$

We note that the factor of 10^{-20} is absorbed into the calculated flux of the table model. Consequently, the normalization should be evaluated without this factor when using the model.

As an initial step, we calculate the spectra in the rest frame of the disk, since including the inclination angle in the full grid would substantially increase the computational time, as the code performs ray-tracing in all iterations and we are interested only in the last one. Once the rest-frame spectra are calculated, we perform ray-tracing for the 3rd iteration only, in order to obtain the spectra in the observer's rest frame.

Model Parameter	Values
Electron density: $n_\mathrm{e}\,(\mathrm{cm}^{-3})$	10^{18}, 10^{19}, 10^{20}, 10^{21}, 10^{22}
Spin parameter: a_*	0.8146, 0.8346, 0.8534, 0.8710, 0.8876, 0.9035, 0.9187, 0.9332, 0.9471, 0.9605, 0.9735, 0.9861, 0.9982
Black hole mass: $M_\mathrm{BH}\,(\mathrm{M}_\odot)$	10
Mass accretion rate: $\dot{M}_\mathrm{BH}\,(10^{18}\,\mathrm{g/s})$	0.14, 0.42, 0.70, 0.84, 0.98, 1.12, 1.26, 1.40, 1.68, 2.1
Inclination angle: $i\,(°)$	30.00, 34.85, 38.87, 42.60, 45.00, 49.50, 52.75, 55.92, 59.02, 62.08, 65.12, 68.15, 71.21, 75.00

Table 3.2: Parameter grids used for the generation of the `zijiRetRad` table model (both blackbody and reflection share the same parameter values).

The full grid contains 9,100 points and was chosen based on parameter values commonly reported in the literature for the XRB 4U 1630–47 during the high-soft state, which serves as the test case for our model (see Section 3.3). The electron density (n_e) spans from 10^{18} to $10^{22}\,\mathrm{cm}^{-3}$; lower densities would yield high ionization parameters, significantly weakening the reflection features. The mass accretion rate ($\dot{M}_\mathrm{BH}$) covers a range of $(0.14 - 2.1)\,10^{18}\,\mathrm{g/s}$. For reference, for a maximally spinning $10\,\mathrm{M}_\odot$ black hole, a mass accretion rate of $1.4 \cdot 10^{18}\,\mathrm{g/s}$ corresponds to approximately 30% of the Eddington accretion rate, defined as:

$$\dot{M}_\mathrm{Edd} = \frac{L_\mathrm{Edd}}{\eta c^2}. \tag{3.5}$$

This value is typically taken as the upper limit of validity of the thin-disk approximation, as higher accretion rates lead to geometrically thick disks that are no longer well described by the Novikov-Thorne model (Riaz, Ayzenberg, et al., 2020a; Riaz, Ayzenberg, et al., 2020b). The black hole spin parameter (a_*) ranges from approximately 0.8 up to the Thorne limit (0.9982), while the mass (M_BH) is fixed to $10\,\mathrm{M}_\odot$. Lastly, the inclination angle (i) is permitted to vary between 30° and 75°.

Finally, we generate two separate additive XSPEC table models for the relativistic spectra: one for the thermal emission (`zijiBB`) and one for the reflection component (`zijiRefl`). Combining these two files, we constructed a single model that incorporates both the reflection and blackbody components, `zijiRetRad`.

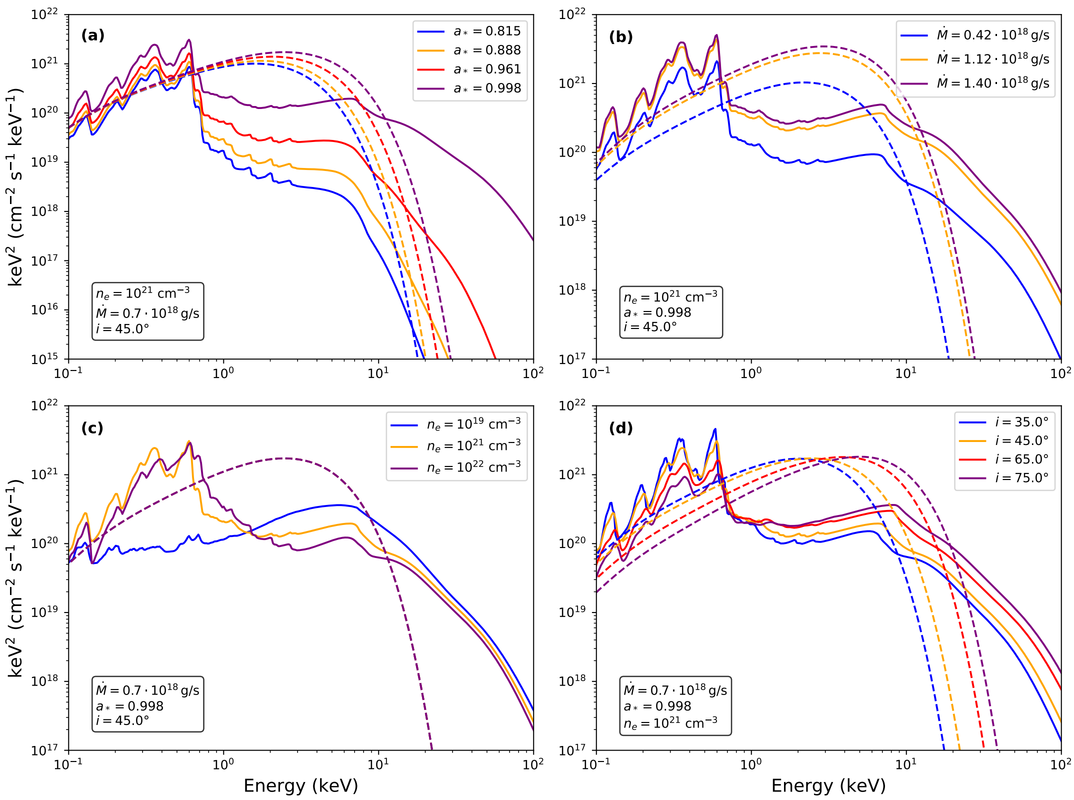

Figure 3.4: Reflection spectra (solid lines) produced by returning radiation (3rd iteration) and black-body spectra (dashed lines) from the `ziji` code for a 10 $M_\odot$ black hole, showing the impact of spin (a), mass accretion rate (b), electron density (c), and inclination angle (d) on the spectra.

The effect of each of the model's parameters on the spectra is illustrated in Fig. 3.4, where the black body and reflection (3rd iteration) spectra are plotted for different values of the spin (a), mass accretion rate (b), electron density (c) and inclination angle (d). In each panel, we vary one parameter while the others remain fixed. The parameter values are chosen simply to demonstrate the qualitative behaviour of the model.

The spin significantly shapes the reflection spectra, as shown in Fig. 3.4(a). Furthermore, in the left panel of Fig. 3.5, we present the returning radiation flux profile in the rest frame of the disk for a 10 $M_\odot$ black hole at different spin values. An increase in spin leads to higher flux returning to each radial bin of the disk, in agreement with the enhanced flux observed at higher spins in Fig. 3.4(a), because $R_{\rm isco}$ moves closer to the black hole. Figure 3.4(b) shows that increasing the mass accretion rate primarily raises the overall flux without significantly affecting the reflection features, while panel (d) illustrates that higher inclinations shift the spectrum to high energies and "wash-out" the emission lines in the soft X-rays due to stronger relativistic effects.

Although the dependence of the flux on spin and mass accretion rate is evident, the effect of the inclination angle is less straightforward. As the inclination increases, the flux decreases in the soft and increases in the hard X-rays. Figure 3.6 shows the integrated flux as a function of inclination for two energy ranges: $0.1 - 100$ keV (total spectrum) and $4 - 100$ keV (hard X-rays), and for the blackbody, reflection, and total components. In the total band, the blackbody flux shows a slight increase with inclination, while the reflection flux decreases rapidly. In the hard X-rays, both components increase at higher inclinations, resulting in a net increase in the total hard X-ray flux. Overall, the total flux in the full energy band decreases slightly with inclination. These trends will be useful when examining parameter correlations in our model via MCMC analysis (see Section 3.3.5).

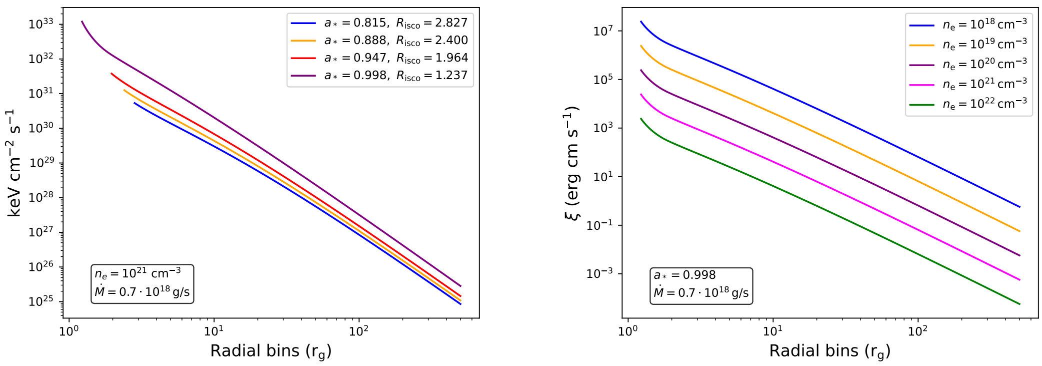

Figure 3.5: Returning radiation flux profile in the rest frame of the disk for different values of the spin parameter (left panel). Ionization profile for different values of the disk electron density (right panel). In both plots $M_{\rm BH} = 10\,{\rm M}_\odot$.

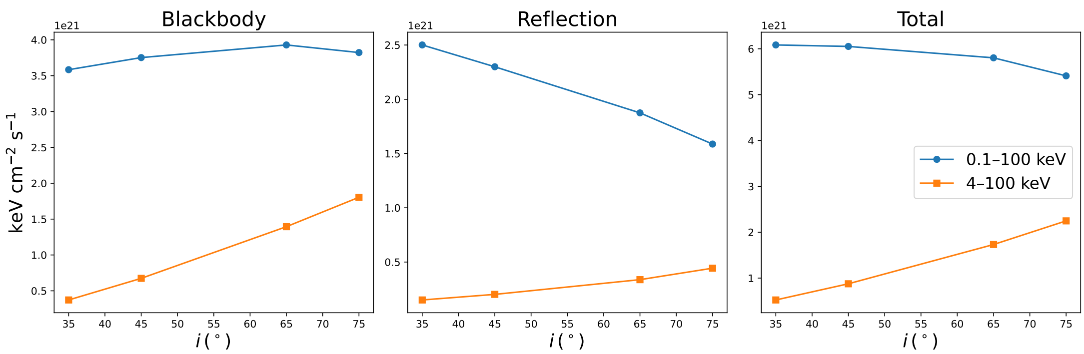

Figure 3.6: Impact of inclination in the integrated flux of blackbody (left), reflection (middle) and total (right) spectra, and for two different energy ranges.

The effect of varying the electron density is shown in Fig. 3.4, panel (c). Even for $n_{\rm e} = 10^{19}\,{\rm cm}^{-3}$, the reflection features are nearly absent, indicating that the disk remains highly ionized. This behavior is consistent with the ionization profile shown in the right panel of Fig. 3.5, which demonstrates that for $n_{\rm e} \lesssim 10^{21}\,{\rm cm}^{-3}$

the disk is strongly ionized. Moreover, the ionization increases toward smaller radii, i.e., closer to the black hole, as expected from the higher temperatures in the inner disk regions. At high ionization parameters the disk surface becomes highly ionized, reducing photoelectric opacity and suppressing fluorescent line production. As a result, characteristic reflection features, particularly the Fe Kα line and absorption edges, are weakened and the spectrum becomes dominated by a smooth Compton-scattered continuum. Finally, the reflection spectra in all panels share a common feature: in the absence of a corona, the Compton hump is weak or even absent, which might be a signature of sources in the high-soft state. A similar result was also reported in previous studies (see, e.g., T. Mirzaev, C. Bambi, et al., 2024; R. M. T. Connors et al., 2021).

3.3 Application of the Model to 4U 1630–47

In the previous section, we described the implementation of the model within XSPEC. To properly evaluate its performance, it is necessary to test the model on real observational data, with particular emphasis on black hole XRBs in the soft spectral state. In this section, we present the full data analysis procedure, outlining all necessary steps required to ensure a robust and reproducible assessment. We then evaluate the significance of our results and the overall performance of the model, and compare it with the current state-of-the-art equivalent model.

3.3.1 Source Selection & Data Reduction

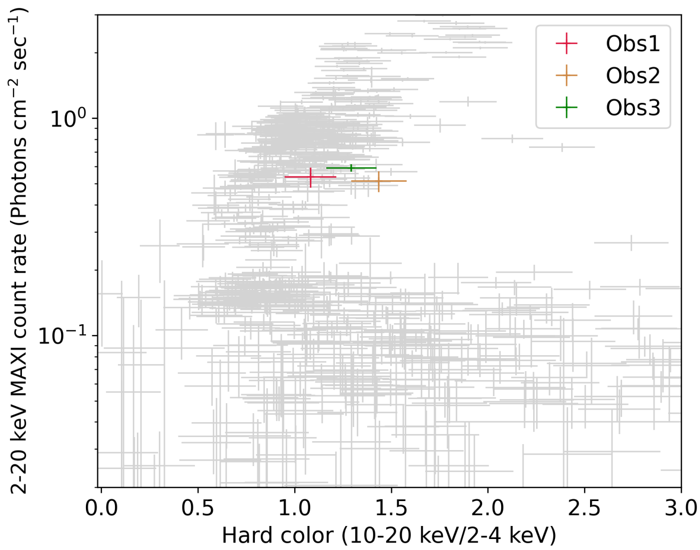

Figure 3.7: The HID using 1-dayaveraged MAXI light curves of 4U 1630–47. The observation considered in this work is Obs1. From Das et al., 2025. Reproduced with permission of the authors.

We proceed by testing our custom table models on the black hole XRB 4U 1630–47, using a *NuSTAR* observation (Obs. ID 80802313002) with an exposure time of 16.2 ksec. The observation was taken while the source was in the high-soft state, as shown in Fig. 3.7, which illustrates the HID. We select 4U 1630–47, as R. M. T. Connors et al., 2021 have shown that in the soft state, returning radiation likely dominates disk illumination.

The *NuSTAR* data were processed using NuSTARDAS v2.1.1 along with the *NuSTAR* CALDB v20230307. Cleaned event files for both FPMA and FPMB were produced using the `nupipeline` tool. The source spectrum was extracted from a circular aperture of 150″ radius centered on the source and was stored in a Pulse Height Amplitude (PHA) file, which contains the observed photon counts as a function of detector channel. The background was extracted from a source-free region of 180″ radius and was stored in a corresponding background (BKG) file. Instrumental response effects were accounted for using the Redistribution Matrix File (RMF), which describes the probability distribution that a photon of a given true energy is detected in a particular detector channel, and the Ancillary Response File (ARF), that encodes the effective collecting area of the telescope as a function of energy. The circular apperture selection procedure is shown in Fig. 3.8. The spectra and associated data products were generated via the `nuproducts` tool. The FPMA and FPMB spectra are grouped to have a minimum count of 30 photons per bin (using the `grppha` command). Spectral fitting was performed with XSPEC v12.15.0 (Arnaud, 1996), using χ^2 statistics to determine the best-fit values and parameter uncertainties.

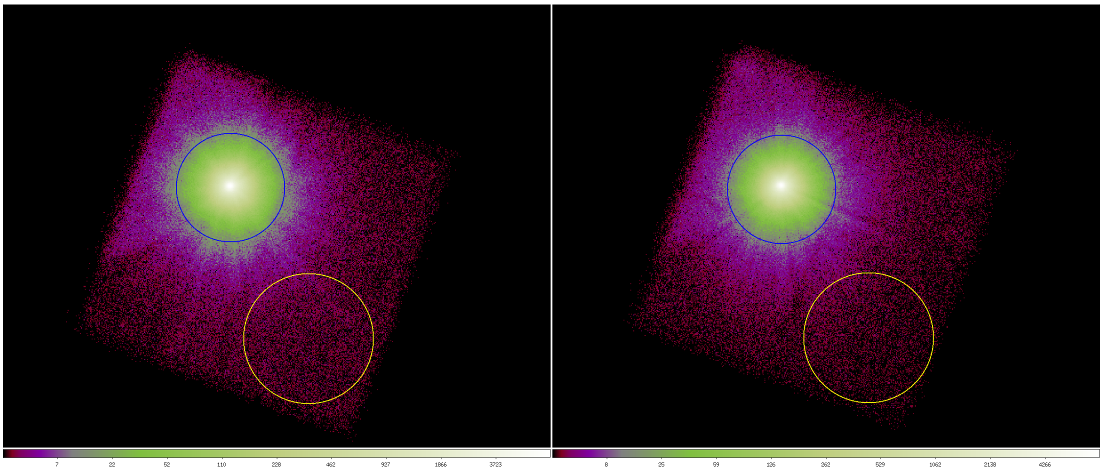

Figure 3.8: Source (blue) and background (yellow) extraction apertures used in the *NuSTAR* data reduction (Obs. ID 80802313002). The source aperture is centered on the target position, while the background aperture is taken from a nearby source-free region. The left and right panels correspond to FPMA and FPMB, respectively.

3.3.2 Spectral Fitting

To motivate the model construction using `zijiRetRad`, we present the process step by step, justifying the inclusion of each component. We fix the black hole mass to $10\,\mathrm{M}_\odot$ (Seifina, Titarchuk, and Shaposhnikov, 2014, indirect mass estimate) and begin with the baseline model (in XSPEC language):

`const*TBabs*zijiBB`,

where `const` accounts for cross-calibration differences between the two $NuSTAR$ detectors (FPMA and FPMB), `TBabs` models interstellar absorption (J. Wilms, Allen, and McCray, 2000), and `zijiBB` is the multicolor blackbody spectrum generated with the `ziji` code. We fix the constant for FPMA to 1.0 and leave the corresponding one for FPMB as a free parameter. The same approach will later be applied when fitting with `relxillNS` (see Section 3.3.4).

The performance of the initial model is shown in the top panel of Fig. 3.9, where we plot the ratio between data and model. Several features remain unresolved: reflection signatures appear above 7 keV, with a sharp rise beyond 10 keV likely due to the onset of the Compton hump, which a pure blackbody model cannot capture. To address this, we added our reflection table model (`zijiRefl`), leading to:

`const*TBabs*zijiRetRad`,

where `zijiRetRad` is the combined reflection and blackbody model. The ratio for this fit is shown in the middle panel of Fig. 3.9. The agreement improves substantially, with most reflection features accounted for. However, clear absorption residuals remain between 6–7 keV, corresponding to disk-wind features previously identified as Fe XXV and Fe XXVI absorption lines at 6.697 keV and 6.966 keV, respectively (Bianchi et al., 2005; A. L. King, J. M. Miller, et al., 2013; Pahari et al., 2018). To model them, we use a custom photoionization table generated with `xstar` (T. Kallman and Bautista, 2001; Das et al., 2025), yielding the model:

`const*TBabs*xstar*zijiRetRad`.

This fit (Fig. 3.9, bottom panel) shows no major systematic deviations in the ratio plot, with a reduced χ^2 of 1.07. The model shown here represents the best-fit obtained with `zijiRetRad`, and the corresponding parameters are listed in Table 3.3 (model 1). To determine the best-fit values and associated uncertainties, we run `steppar` on each parameter, followed by `error` to estimate confidence intervals at the 90% level.

3.3.3 Results & Discussion

We report a rapidly spinning black hole ($a_* \sim 0.99$) and a disk inclination of $i \sim 53°$. The hydrogen column density is estimated to be $N_\mathrm{H} \sim 1.3 \cdot 10^{23}\,\mathrm{cm}^{-2}$, while the mass accretion rate is $\dot{M}_\mathrm{BH} \sim 0.83 \cdot 10^{18}$ g/s, corresponding to approximately

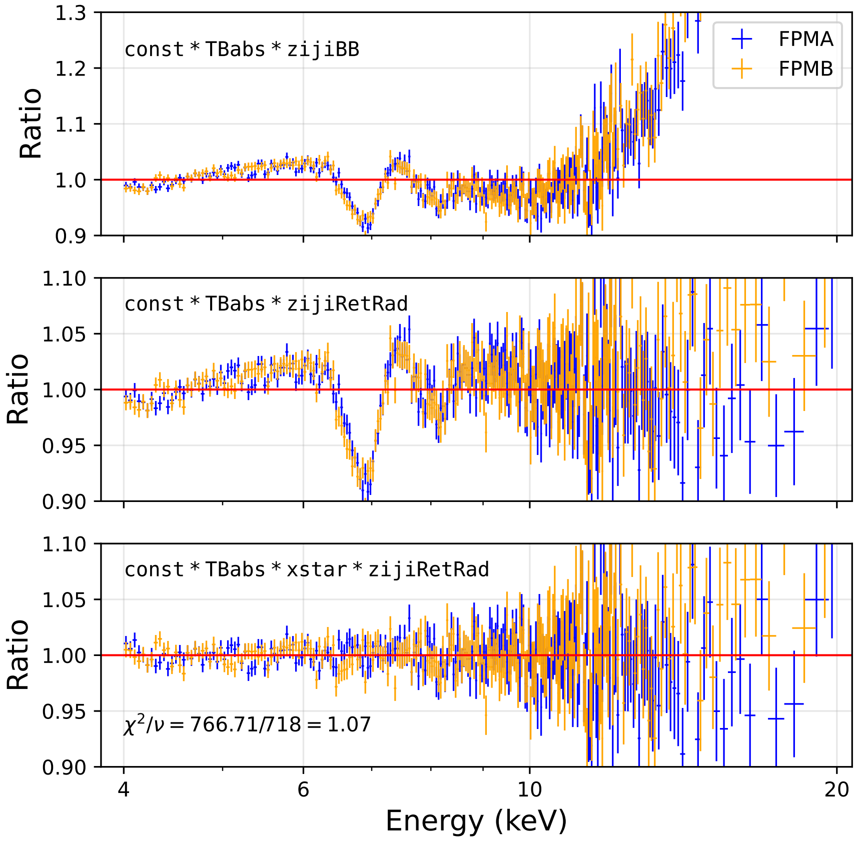

Figure 3.9: Ratio plots for the different models utilized during model build-up using `zijiRetRad`. The respective models are shown in the upper part of each panel. The lower panel shows the bets-fit model alongside the reduced χ^2 obtained. Blue and orange colors correspond to FPMA and FPMB respectively.

15% $\dot{\mathrm{M}}_{\mathrm{Edd}}$. Moreover, we infer a high electron density of $n_e \sim 10^{21}\,\mathrm{cm}^{-3}$. Finally, the distance to the source inferred from our analysis is $D \sim 8.2\,\mathrm{kpc}$.

The parameter values obtained in our analysis are generally consistent with those reported in the literature. Kuulkers et al., 1998, R. M. T. Connors et al., 2021, Das et al., 2025, and Tomsick, Lapshov, and Kaaret, 1998 all reported high hydrogen column densities along the line of sight, with $N_{\mathrm{H}} \sim (4-12)\cdot 10^{22}\,\mathrm{cm}^{-2}$. Gatuzz et al., 2019 reported a value closer to $10^{23}\,\mathrm{cm}^{-2}$, while R. M. T. Connors et al., 2021 adopted $N_{\mathrm{H}} \sim 1.4\cdot 10^{23}\,\mathrm{cm}^{-2}$, similar to our result. They justified this choice by pointing to the uncertainties in N_{H} derived from X-ray data (Tomsick, Lapshov, and Kaaret, 1998; Tomsick and Kaaret, 2000; Gatuzz et al., 2019), as well as the presence of dust scattering along the line of sight (Kalemci, Maccarone, and Tomsick, 2018). The mass accretion rate is consistent with the value reported by Das et al., 2025 ($\dot{M}_{\mathrm{BH}} \sim 15-20\%\,\dot{\mathrm{M}}_{\mathrm{Edd}}$).

A high inclination has been reported by Tomsick, Lapshov, and Kaaret, 1998, Seifina, Titarchuk, and Shaposhnikov, 2014, and R. M. T. Connors et al., 2021, with values in the range $60^\circ < i < 70^\circ$. However, R. M. T. Connors et al., 2021 also found a lower estimate of $i \sim 37^\circ$ using `relxillNS`, while reflection modeling by A. L. King, Walton, et al., 2014 provided an estimate of $i \sim 64^\circ$. Recent analyses by Draghis et al., 2024 and Das et al., 2025 reported somewhat lower inclination values of $i \sim 55^\circ$, with the former exhibiting larger uncertainties; these values are closer to the one obtained in our analysis. The spin of the black hole has also been estimated to be high. A. L. King, Walton, et al., 2014 found $a_* = 0.985^{+0.005}_{-0.014}$, and R. M. T. Connors et al., 2021 reported a similar value, although lower estimates have also appeared in the literature, e.g. $a_* = 0.857^{+0.095}_{-0.211}$ (Draghis et al., 2024), $0.85^{+0.07}_{-0.07}$ (R. M. T. Connors et al., 2021), and $0.837^{+0.067}_{-0.156}$ (Das et al., 2025).

The high electron density we find in our analysis is consistent with the results of R. M. T. Connors et al., 2021, who reported $n_e > 10^{20}\,\mathrm{cm}^{-3}$ across all spectral states. As discussed earlier (see Fig. 3.4(c)), such high densities are required for the reflection features to be present. In addition, the parameters we obtain for the `xstar` model are in good agreement with those reported by Das et al., 2025, analyzing the same observation.

Component	Parameter	Model 1	Model 2
`TBabs`	$N_\mathrm{H}\,(10^{22}\,\mathrm{cm}^{-2})$	$13.35^{+0.18}_{-0.23}$	$13.60^{+0.15}_{-0.18}$
`xstar`	$column\,(10^{23})$	$1.10^{+0.16}_{-0.13}$	$1.01^{+0.12}_{-0.07}$
	$rlog\xi$	$4.01^{+0.10}_{-0.09}$	$3.95^{+0.09}_{-0.05}$
`zijiRetRad`	$n_\mathrm{e}\,(10^{21}\,\mathrm{cm}^{-3})$	$1.00^{+1.33}_{-0.34}$	$0.101^{+0.076}_{-0.004}$
	a_*	$0.9878^{+0.0002}_{-0.0003}$	$0.98653^{+0.00006}_{-0.00008}$
	$M_\mathrm{BH}\,(\mathrm{M}_\odot)$	10^*	10^*
	$\dot{M}_\mathrm{BH}\,(10^{18}\,\mathrm{g/s})$	$0.83^{+0.04}_{-0.08}$	$1.235^{+0.007}_{-0.008}$
	$i\,(^\circ)$	$52.6^{+0.4}_{-0.7}$	$46.6^{+0.2}_{-0.3}$
	$D\,(\mathrm{kpc})$	$8.19^{+0.16}_{-0.43}$	10^*
`constant`	C_FPMA	$0.987^{+0.002}_{-0.002}$	$0.987^{+0.002}_{-0.002}$
χ^2/ν		$766.71/718 = 1.07$	$803.05/719 = 1.12$

Table 3.3: Best-fit values obtained using `zijiRetRad`. The asterisk ($*$) denotes that the parameter is fixed at this value.

The distance inferred in our analysis is lower than the values reported by Kalemci, Diaz Trigo, et al., 2025 and Kalemci, Maccarone, and Tomsick, 2018 ($\sim 11.5\,\mathrm{kpc}$) when modeling the dust-scattering halo, as well as the 10 kpc distance commonly adopted in the literature (see, e.g., Seifina, Titarchuk, and Shaposhnikov, 2014; Augusteijn, Kuulkers, and van Kerkwijk, 2001). To provide

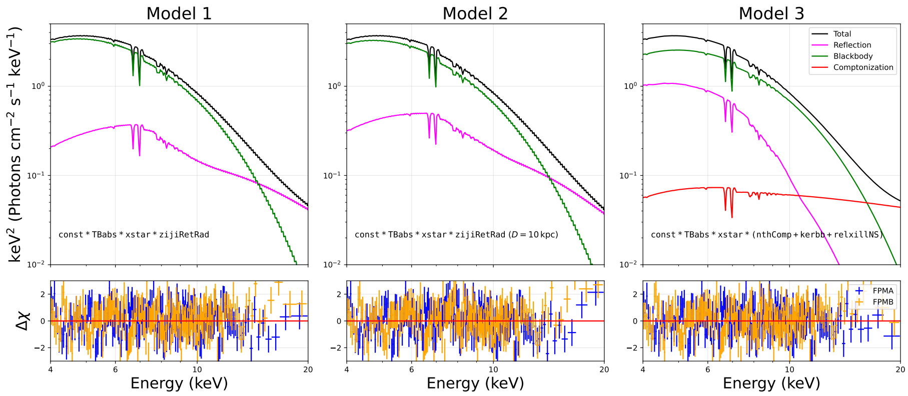

Figure 3.10: Model components (upper panels) and $\Delta\chi = (\text{data} - \text{model})/\text{error}$ (lower panels) for the best-fit models obtained with `zijiRetRad` (left panels with D free and middle panels with $D = 10\,\text{kpc}$) and with `relxillNS` (right panels). The green, magenta, red, and black curves correspond to the blackbody, reflection, Comptonization, and total spectra, respectively. In the upper left and middle (right) panels, the reflection and blackbody components correspond to `zijiRefl` (`relxillNS`) and `zijiBB` (`kerrbb`), while the Comptonization component (`nthComp`) is present only in the `relxillNS` panel. The total model is indicated at the bottom of each upper panel.

a direct comparison, we repeat our analysis using the same spectral model but fixing the distance to 10 kpc, and refit the data. The best-fit parameter values for this configuration are reported in the last column of Table 3.3. As in our baseline fit, the solution favors a rapidly rotating black hole; however, the inclination angle is lower and the inferred mass accretion rate is higher. We do not discuss all parameter changes in detail, as this is beyond the scope of the present work, but we note that the shifts are consistent with the parameter correlations revealed by the MCMC analysis (see Fig. 3.12). The corresponding model components and residuals are shown in the middle panel of Fig. 3.10. In this case, the residuals display a clear increasing trend at high energies, indicating that the model struggles to reproduce the observed high-energy tail.

3.3.4 Comparison with `relxillNS`

To place our results in context, we compare `zijiRetRad` with `relxillNS` (García, Thomas Dauser, et al., 2022), a model widely applied for returning radiation (Riley M. T. Connors et al., 2020; R. M. T. Connors et al., 2021). It is worth noting once again that `relxillNS` is not a true self-irradiation model and was initially created for neutron star reflection spectroscopy: instead of using the intrinsic disk spectrum, it illuminates the accretion disk with a single-temperature blackbody. Although not self consistent, it can mimic the spectrum of returning radiation and this is why it is extensively used in the literature. While `zijiRetRad` relies on the well-tested `reflionx` (Ross and Fabian, 2005) radiative transfer code, `relxillNS` uses `xillverNS` (García, Thomas Dauser, et al., 2022). The key difference is that `xillverNS` treats the emission angle as an explicit model parameter, allowing `relxillNS` to calculate the relativistic spectra taking into account (with some approximations) that the emission angle is not equal to the inclination angle of the disk because of the light bending. In contrast, `reflionx` adopts an angle-averaged approach. Since `relxillNS` has been extensively studied in the literature, we do not present its setup in detail here. We fit the same observational data with `relxillNS`, and the resulting best-fit model is:

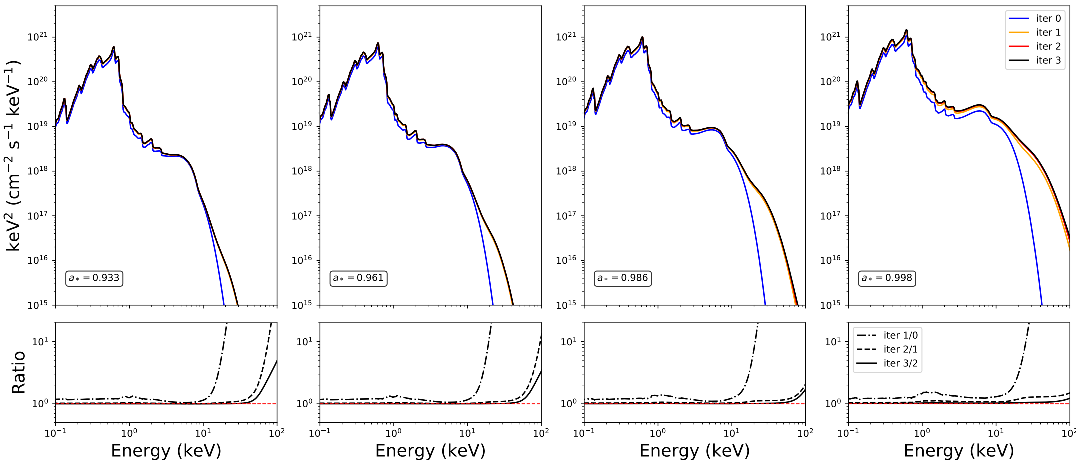

Figure 3.11: Relativistic reflection spectra generated with the `ziji` code for different numbers of iterative reflections (0–3) and spin values (upper panels). The bottom panels show the ratio between the flux of each successive iteration. Model parameters were randomly selected to illustrate the qualitative behaviour of the spectrum as the number of iterations increase (in all panels: $M_{\rm BH} = 10\,{\rm M}_{\odot}, \dot{M}_{\rm BH} = 0.3 \cdot 10^{18}\,{\rm g/s}, n_{\rm e} = 10^{22}\,{\rm cm}^{-3}, i = 45°$). Iteration 0 represents the reflection spectra produced solely by the direct returning radiation of the thermal component, while iterations 1–3 show the reflection spectra that also include the returning radiation of the reflection component for the corresponding number of iterations.

`const*TBabs*xstar*(nthComp+kerrbb+relxillNS)`,

where `nthComp` accounts for the Comptonized emission (assuming a multicolor disk blackbody seed spectrum; *inp_type* = 1) and `kerrbb` for the multicolor blackbody. We fix the power-law index, $\Gamma = 2.5$, and the electron temperature, $kT_{\rm e} = 100\,{\rm keV}$, of `nthComp`, leaving only the normalization as a free parameter. Moreover, the distance is fixed at $D = 10\,{\rm kpc}$ (Seifina, Titarchuk, and Shaposhnikov, 2014; Augusteijn, Kuulkers, and van Kerkwijk, 2001; see also Kalemci, Diaz Trigo, et al., 2025, for a different estimate), since it cannot be simultaneously constrained with the mass accretion rate within this model. The mass is fixed at $10\,\mathrm{M}_\odot$ (Seifina, Titarchuk, and Shaposhnikov, 2014) and the iron abundance at the solar value ($A_{\mathrm{Fe}} = 1$), ensuring consistency with the prior analysis using `zijiRetRad`. For reference, `zijiBB` and `kerrbb` are essentially equivalent.

The best-fit values obtained with `relxillNS` are listed in Table 3.4. They are broadly consistent with earlier studies and with the results from `zijiRetRad`, although some differences are worth highlighting. In particular, `relxillNS` returns lower electron densities and accretion rates. We obtain $\dot{M}_{\mathrm{BH}} \sim 0.58 \cdot 10^{18}\,\mathrm{g/sec}$, corresponding to $\sim 13\%\,\dot{\mathrm{M}}_{\mathrm{Edd}}$. The electron density lies between $\sim 10^{15} - 10^{18}\,\mathrm{cm}^{-3}$, whereas `zijiRetRad` requires densities around $10^{21}\,\mathrm{cm}^{-3}$. A detailed examination of all parameter values is beyond the scope of this study.

Component	Parameter	Model 3
`TBabs`	$N_{\mathrm{H}}\,(10^{22}\,\mathrm{cm}^{-2})$	$12.3^{+0.3}_{-0.5}$
`xstar`	$column\,(10^{23})$	$1.07^{+0.17}_{-0.14}$
	$rlog\xi$	$4.01^{+0.10}_{-0.10}$
`nthComp`	$Gamma$	2.5^{*}
	$kT_{\mathrm{e}}\,(\mathrm{keV})$	100^{*}
	$norm\,(10^{-2})$	$4.84^{+0.17}_{-0.16}$
`kerrbb`	a_*	$0.998^{p}_{-0.005}$
	$i\,(^\circ)$	$56.15^{+1.05}_{-1.08}$
	$\dot{M}_{\mathrm{BH}}\,(10^{18}\,\mathrm{g/s})$	$0.58^{+0.04}_{-0.05}$
	$M_{\mathrm{BH}}\,(\mathrm{M}_\odot)$	10^{*}
	$D\,(\mathrm{kpc})$	10^{*}
`relxillNS`	$kT_{\mathrm{bb}}\,(\mathrm{keV})$	$0.89^{+0.03}_{-0.03}$
	$log\xi$	$2.46^{+0.21}_{-0.25}$
	$log(n_{\mathrm{e}})\,(\mathrm{cm}^{-3})$	$17.5^{+0.7}_{p}$
	A_{Fe}	1.0^{*}
	$norm\,(10^{-2})$	$1.9^{+0.6}_{-0.4}$
`constant`	C_{FPMA}	$0.987^{+0.002}_{-0.002}$
χ^2/ν		$758.26/715 = 1.06$

Table 3.4: Same as Table 3.3, but for `relxillNS`. The superscript (subscript) p indicates that the parameter is constrained at the maximum (minimum) value permitted by the model.

The model components and residuals are shown in Fig. 3.10, where the left panels correspond to `zijiRetRad` and the right panels correspond to `relxillNS`. The most notable difference between the two models is that the `zijiRetRad` reflection spectrum is significantly harder at high energies relative to `relxillNS`. Consequently, only the latter one requires an additional weak coronal component to produce the observed high-energy tail. In the case of `zijiRetRad`, the hard excess arises naturally from the iterative reflection included in the model, which is absent in `relxillNS`. Figure 3.11 shows the relativistic reflection spectra for different numbers of iterations (0–3) and for varying black hole spins. The high-energy tail becomes progressively harder with increasing iteration number and black hole spin. As the disk ($R_{\rm isco}$) moves closer to the black hole, gravitational light bending and Doppler blueshift increase the flux reaching the disk from its innermost regions, resulting in a harder high-energy spectrum for the iterative reflection. Interestingly, without accounting for a coronal component, producing a high-energy tail in the reflection spectrum requires pushing the spin parameter to high values. As a result, neglecting the corona could lead to overestimating the inferred spin in some cases, when such tails are present in the data. However, in our case, we verified that including a coronal component alongside `zijiRetRad` does not improve the quality of the fit.

3.3.5 MCMC Analysis

To characterize the posterior distributions of the best-fit parameters listed in Table 3.3, we employed the Markov Chain Monte Carlo[5] (MCMC) implementation in XSPEC, which uses the affine-invariant ensemble sampler of Goodman and Weare, 2010. We initialized 50 walkers and evolved the chains for 10,000,000 steps, discarding the first 100,000 steps as burn-in. The corner plot for the best fit model parameters listed in Table 3.3 is shown in Fig. 3.12.

We find several strong parameter correlations in the MCMC posterior. There is strong correlation between the two parameters of the `xstar` model; column density and ionization parameter. Physically, a higher ionization corresponds to a larger fraction of fully stripped iron and therefore a higher column density is required to produce the same absorption line. We also identify a significant correlation between the mass accretion rate and the source distance, as both parameters effectively act as scaling factors in the model (see Fig. 3.4(b)). An increase in the accretion rate therefore favors a corresponding increase in the distance, and vice versa.

Furthermore, the black hole spin and the inclination are correlated, such that higher spin values favor larger inclinations. Increasing the spin decreases $R_{\rm isco}$, thereby increasing the inner disk flux. A higher inclination reduces the observed flux because the projected area along the line of sight decreases roughly as $\cos i$ ($i = 0°$ is face on and $i = 90°$ is edge on), although this effect is partially offset

[5]The details of MCMC are beyond the scope of this thesis. For an introduction, see e.g. Hjorth-Jensen, 2015.

by relativistic Doppler boosting at high inclinations. Conversely, increasing the spin reduces the inferred mass accretion rate. Roughly speaking, the emitted flux from a thin disk scales as $F \propto \dot{M}_{\rm BH}/R_{\rm isco}^2$; since a higher spin black hole has a smaller $R_{\rm isco}$, the same observed flux can be reproduced with a lower $\dot{M}_{\rm BH}$. Finally, both the mass accretion rate and the distance show correlations with the inclination angle, which can be understood from the flux degeneracy discussed above. In contrast, increasing the distance reduces the observed flux, favoring a smaller inclination to reproduce the same flux.

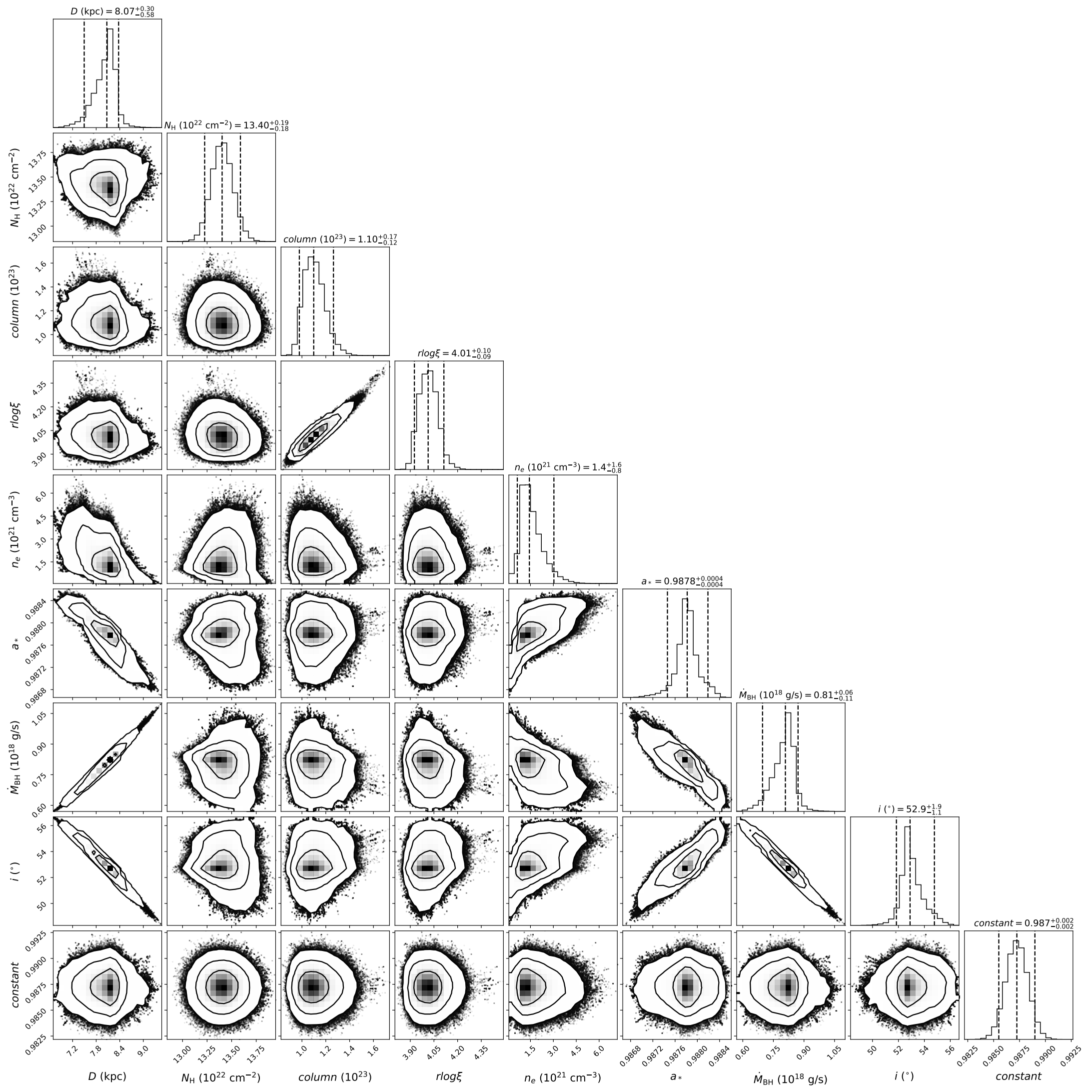

Figure 3.12: Corner plot for the best fit model using `zijiRetRad`. The error values of each of the parameter corresponds to 90% confidence level. The contours correspond to 68%, 95% and 97.5% confidence levels.

Interestingly, the MCMC posterior reveals an anti-correlation between the mass accretion rate and the inclination angle, such that higher accretion rates favor lower inclinations. At first glance, this appears counterintuitive, as a higher intrinsic luminosity would naively be expected to be compensated by a more edge-on geometry. However, this intuition assumes that inclination only affects the overall flux normalization. In relativistic disk models, the inclination also strongly influences the spectral shape through Doppler boosting, gravitational redshift, and angular emission effects. Increasing the inclination enhances relativistic boosting and hardens the spectrum, which can overproduce high-energy flux when combined with a higher accretion rate. Consequently, the MCMC prefers lower inclinations.

It is worth noting that the posterior distributions presented here are marginalized distributions, obtained by integrating the full posterior over parameters that are not explicitly shown. For example, the joint posterior distribution of two parameters (θ_1, θ_2) is given by:

$$P(\theta_1, \theta_2 \,|\, \mathrm{data}) = \int P(\theta_1, \theta_2, \theta_3 ... \,|\, \mathrm{data})\, d\theta_3 ..., \tag{3.6}$$

where the integration is performed over all remaining model parameters. As a result, correlations observed in two-dimensional posterior projections reflect averaged behavior over the allowed ranges of all other parameters, rather than conditional relationships at fixed values. Overall, these correlations reflect intrinsic degeneracies in a flux-calibrated model without a free normalization and do not affect our main conclusions.

Chapter 4

Conclusions & Future Work

This study presents the first XSPEC table model that isolates the reflection spectrum produced by returning radiation from the accretion disk, excluding any contribution from the corona. When applied to the black hole XRB 4U 1630–47 during the soft spectral state, the model provides a good fit to the data ($\chi^2/\nu = 1.07$). The best-fit indicates a high black hole spin ($a_* \sim 0.99$), a disk inclination of $i \sim 53°$, an increased electron density ($n_\mathrm{e} \sim 10^{21}\,\mathrm{cm}^{-3}$) and a mass accretion rate of $\dot{M}_\mathrm{BH} \sim 15\%\,\dot{\mathrm{M}}_\mathrm{Edd}$, broadly consistent with previous studies. The inferred source distance, $D \sim 8.2\,\mathrm{kpc}$, is lower than the $\sim 10\,\mathrm{kpc}$ value commonly adopted in the literature, indicating a modest difference relative to earlier estimates.

We compared our model with the widely used `relxillNS`, a model that mimics returning radiation. Our analysis shows that `relxillNS` requires a weak corona to adequately describe the data, in contrast to `zijiRetRad`. The latter produces a harder reflection spectrum at high energies and can naturally give rise to a high-energy tail without needing an additional Comptonized component. This behavior arises from the iterative reflection implemented in the `ziji` code, as well as from the high spin value inferred by our model.

Our model is, of course, a simplification, as we neglect the corona entirely, even though it is thought to be weak or even absent in soft states. Nevertheless, the results demonstrate that returning radiation alone can account for the observed spectra and should therefore be considered an important component during the high-soft state.

A natural next step would be to include a weak corona self-consistently, in order to assess the relative contributions of coronal emission and self-irradiation. Extending the parameter grid of our model would also be valuable, particularly by including lower spin and mass values. However, as previously discussed, slower rotation would reduce the impact of returning radiation because the inner edge of the disk (R_isco) moves outward. Moreover, since the code can accommodate any stationary, axisymmetric, and asymptotically flat spacetime, it could be extended to employ parametrized Kerr-like metrics, such as the Johannsen metric (Johannsen, 2013), in order to test the Kerr hypothesis. Furthermore, it would be crucial to perform a systematic analysis, such as varying the iron abundance (A_{Fe}) in the model, to assess how model-dependent our results are. To further generalize these findings, it will be necessary to extend the parameter space and apply `zijiRetRad` to additional sources in the soft state. Table 4.1 lists sources whose spectra have been speculated to be dominated by self-irradiation of the disk, providing a starting point for this analysis. Ultimately, the goal is to make the model publicly available within the XSPEC community.

Source	Reference
4U 1543–47	Zhao et al., 2024
EXO 1846–031	Y. Wang et al., 2021
XTE J1550–564	Riley M. T. Connors et al., 2020

Table 4.1: Candidate XRB sources dominated by returning radiation, with corresponding references.

List of Figures

List of Tables

72

Bibliography

Abbott, B. P., R. Abbott, T. D. Abbott, M. R. Abernathy, et al. (Feb. 2016). “Observation of Gravitational Waves from a Binary Black Hole Merger”. In: *Phys. Rev. Lett.* 116 (6), p. 061102. DOI: 10.1103/PhysRevLett.116.061102. URL: https://link.aps.org/doi/10.1103/PhysRevLett.116.061102.

Abbott, B. P., R. Abbott, T. D. Abbott, S. Abraham, et al. (July 2019). “GWTC-1: A Gravitational-Wave Transient Catalog of Compact Binary Mergers Observed by LIGO and Virgo during the First and Second Observing Runs”. In: *Physical Review X* 9.3, 031040, p. 031040. DOI: 10.1103/PhysRevX.9.031040. arXiv: 1811.12907 [astro-ph.HE].

Abdikamalov, A. B. et al. (2020). “Testing the Kerr Black Hole Hypothesis Using X-Ray Reflection Spectroscopy and a Thin Disk Model with Finite Thickness”. In: *ApJ* 899, p. 80. DOI: 10.3847/1538-4357/aba625.

Abdikamalov, Askar B. et al. (Feb. 2024). *blackray*. Version v1.0.1. DOI: 10.5281/zenodo.10673859. URL: https://doi.org/10.5281/zenodo.10673859.

Arnaud, K. A. (Jan. 1996). “XSPEC: The First Ten Years”. In: *Astronomical Data Analysis Software and Systems V*. Ed. by G. H. Jacoby and J. Barnes. Vol. 101. ASP Conf. Ser. P. 17.

Augusteijn, T., E. Kuulkers, and M. H. van Kerkwijk (Aug. 2001). “The IR counterpart of the black-hole candidate 4U 1630-47”. In: *A&A* 375, pp. 447–454. DOI: 10.1051/0004-6361:20010855. arXiv: astro-ph/0107337 [astro-ph].

Bambi, C. (2017). *Black Holes: A Laboratory for Testing Strong Gravity*. Springer. ISBN: 978-981-10-4523-3. DOI: 10.1007/978-981-10-4524-0.

— (2024). “Black hole X-ray spectra: notes on the relativistic calculations”. In: *arXiv* 2408.12262. DOI: 10.48550/arXiv.2408.12262.

Bambi, C. et al. (2021). “Towards Precision Measurements of Accreting Black Holes Using X-Ray Reflection Spectroscopy”. In: *Space Sci. Rev.* 217, p. 65. DOI: 10.1007/s11214-021-00841-8.

Bambi, Cosimo (2017). “X-Ray Reflection Spectroscopy”. In: *Black Holes: A Laboratory for Testing Strong Gravity*. Singapore: Springer Singapore, pp. 153–179. ISBN: 978-981-10-4524-0. DOI: 10.1007/978-981-10-4524-0_8. URL: https://doi.org/10.1007/978-981-10-4524-0_8.

— (June 2018a). “Astrophysical Black Holes: A Compact Pedagogical Review”. In: *Annalen der Physik* 530.6, p. 1700430. DOI: 10.1002/andp.201700430. arXiv: 1711.10256 [gr-qc].

Bambi, Cosimo (2018b). *Introduction to General Relativity. A Course for Undergraduate Students of Physics*. DOI: 10.1007/978-981-13-1090-4.

Bardeen, J. M., B. Carter, and S. W. Hawking (June 1973). "The four laws of black hole mechanics". In: *Communications in Mathematical Physics* 31.2, pp. 161–170. DOI: 10.1007/BF01645742.

Bardeen, James M. (Apr. 1970). "Kerr Metric Black Holes". In: *Nature* 226.5240, pp. 64–65. DOI: 10.1038/226064a0.

Bardeen, James M., William H. Press, and Saul A. Teukolsky (Dec. 1972). "Rotating Black Holes: Locally Nonrotating Frames, Energy Extraction, and Scalar Synchrotron Radiation". In: *ApJ* 178, pp. 347–370. DOI: 10.1086/151796.

Belczynski, Krzysztof et al. (May 2010). "On the Maximum Mass of Stellar Black Holes". In: *ApJ* 714.2, pp. 1217–1226. DOI: 10.1088/0004-637X/714/2/1217. arXiv: 0904.2784 [astro-ph.SR].

Belloni, T. et al. (Sept. 2005). "The evolution of the timing properties of the black-hole transient GX 339-4 during its 2002/2003 outburst". In: *A&A* 440.1, pp. 207–222. DOI: 10.1051/0004-6361:20042457. arXiv: astro-ph/0504577 [astro-ph].

Bianchi, S. et al. (2005). "Fe xxv and Fe xxvi lines from low-velocity, photoionized gas in the X-ray spectra of active galactic nuclei". In: *MNRAS* 357, p. 599. DOI: 10.1111/j.1365-2966.2005.08661.x.

Birkhoff, George David and Rudolph Ernest Langer (1923). *Relativity and modern physics*.

Blandford, R. D. and R. L. Znajek (May 1977). "Electromagnetic extraction of energy from Kerr black holes." In: *MNRAS* 179, pp. 433–456. DOI: 10.1093/mnras/179.3.433.

Bolton, C. T. (Feb. 1972). "Identification of Cygnus X-1 with HDE 226868". In: *Nature* 235.5336, pp. 271–273. DOI: 10.1038/235271b0.

Boyer, Robert H. and Richard W. Lindquist (Feb. 1967). "Maximal Analytic Extension of the Kerr Metric". In: *Journal of Mathematical Physics* 8.2, pp. 265–281. DOI: 10.1063/1.1705193.

Cárdenas-Avendaño, Alejandro, Menglei Zhou, and Cosimo Bambi (June 2020). "Modeling uncertainties in x-ray reflection spectroscopy measurements. II. Impact of the radiation from the plunging region". In: *Phys. Rev. D* 101.12, 123014, p. 123014. DOI: 10.1103/PhysRevD.101.123014. arXiv: 2005.06719 [astro-ph.HE].

Carter, B. (Feb. 1971). "Axisymmetric Black Hole Has Only Two Degrees of Freedom". In: *Phys. Rev. Lett.* 26.6, pp. 331–333. DOI: 10.1103/PhysRevLett.26.331.

Casares, J. and P. G. Jonker (Sept. 2014). "Mass Measurements of Stellar and Intermediate-Mass Black Holes". In: *Space Sci. Rev.* 183.1-4, pp. 223–252. DOI: 10.1007/s11214-013-0030-6. arXiv: 1311.5118 [astro-ph.HE].

Colbert, Edward J. M. and Richard F. Mushotzky (July 1999). "The Nature of Accreting Black Holes in Nearby Galaxy Nuclei". In: *ApJ* 519.1, pp. 89–107. DOI: 10.1086/307356. arXiv: astro-ph/9901023 [astro-ph].

Coleman Miller, M. and E. J. M. Colbert (2004). "Intermediate-mass Black Holes". In: *International Journal of Modern Physics D* 13.01, pp. 1–64. DOI: 10.1142/S0218271804004426.

Connors, R. M. T. et al. (2021). "Reflection Modeling of the Black Hole Binary 4U 1630–47: The Disk Density and Returning Radiation". In: *ApJ* 909, p. 146. DOI: 10.3847/1538-4357/abdd2c.

Connors, Riley M. T. et al. (Mar. 2020). "Evidence for Returning Disk Radiation in the Black Hole X-Ray Binary XTE J1550-564". In: *ApJ* 892.1, 47, p. 47. DOI: 10.3847/1538-4357/ab7afc. arXiv: 2002.11873 [astro-ph.HE].

Cunningham, C. (1976). "Returning radiation in accretion disks around black holes". In: *ApJ* 208, p. 534. DOI: 10.1086/154636.

Cunningham, C. T. (Dec. 1975). "The effects of redshifts and focusing on the spectrum of an accretion disk around a Kerr black hole." In: *ApJ* 202, pp. 788–802. DOI: 10.1086/154033.

Dabrowski, Y. et al. (1997). "The profile and equivalent width of the X-ray iron emission line from a disc around a Kerr black hole". In: *MNRAS* 288, p. L11. DOI: 10.1093/mnras/288.1.L11.

Das, D. et al. (2025). "Spin Constraints on 4U 1630-47 via combined Continuum Fitting and Reflection methods: a comparative study using Frequentist and Bayesian statistics". In: *arXiv* 2509.09481. DOI: 10.48550/arXiv.2509.09481.

Dauser, T., J. Garcia, et al. (2013). "Irradiation of an accretion disc by a jet: general properties and implications for spin measurements of black holes". In: *MNRAS* 430, p. 1694. DOI: 10.1093/mnras/sts710.

Dauser, T., J. A. Garcia, et al. (2022). "The effect of returning radiation on relativistic reflection". In: *MNRAS* 514, p. 3965. DOI: 10.1093/mnras/stac1593.

Dauser, T., J. Wilms, et al. (Dec. 2010). "Broad emission lines for a negatively spinning black hole". In: *MNRAS* 409.4, pp. 1534–1540. DOI: 10.1111/j.1365-2966.2010.17393.x. arXiv: 1007.4937 [astro-ph.HE].

De Rosa, A. et al. (2019). "Accretion in strong field gravity with eXTP". In: *Sci. China Phys. Mech. Astron.* 62, p. 29504. DOI: 10.1007/s11433-018-9297-0.

Ding, Yuanze et al. (Oct. 2024). "Next-generation Accretion Disk Reflection Model: High-density Plasma Effects". In: *ApJ* 974.2, 280, p. 280. DOI: 10.3847/1538-4357/ad76a1. arXiv: 2409.00253 [astro-ph.HE].

Done, Chris, Marek Gierliński, and Aya Kubota (Dec. 2007). "Modelling the behaviour of accretion flows in X-ray binaries. Everything you always wanted to know about accretion but were afraid to ask". In: *A&A Rev.* 15.1, pp. 1–66. DOI: 10.1007/s00159-007-0006-1. arXiv: 0708.0148 [astro-ph].

Dovciak, M., V. Karas, and T. Yaqoob (2004). "An Extended Scheme for Fitting X-Ray Data with Accretion Disk Spectra in the Strong Gravity Regime". In: *ApJS* 153, p. 205. DOI: 10.1086/421115.

Dovčiak, M. et al. (Nov. 2008). "Thermal disc emission from a rotating black hole: X-ray polarization signatures". In: *MNRAS* 391.1, pp. 32–38. DOI: 10.1111/j.1365-2966.2008.13872.x. arXiv: 0809.0418 [astro-ph].

Draghis, Paul A. et al. (July 2024). "Systematically Revisiting All NuSTAR Spins of Black Holes in X-Ray Binaries". In: *ApJ* 969.1, 40, p. 40. DOI: 10.3847/1538-4357/ad43ea. arXiv: 2311.16225 [astro-ph.HE].

Einstein, A. (Jan. 1916). "Die Grundlage der allgemeinen Relativitätstheorie". In: *Annalen der Physik* 354.7, pp. 769–822. DOI: 10.1002/andp.19163540702.

Event Horizon Telescope Collaboration, Kazunori Akiyama, Antxon Alberdi, Walter Alef, Juan Carlos Algaba, et al. (May 2022). "First Sagittarius A* Event Horizon Telescope Results. I. The Shadow of the Supermassive Black Hole in the Center of the Milky Way". In: *ApJ* 930.2, L12, p. L12. DOI: 10.3847/2041-8213/ac6674.

Event Horizon Telescope Collaboration, Kazunori Akiyama, Antxon Alberdi, Walter Alef, Keiichi Asada, et al. (Apr. 2019). "First M87 Event Horizon Telescope Results. I. The Shadow of the Supermassive Black Hole". In: *ApJ* 875.1, L1, p. L1. DOI: 10.3847/2041-8213/ab0ec7. arXiv: 1906.11238 [astro-ph.GA].

Fabian, A. C., K. Iwasawa, et al. (Sept. 2000). "Broad Iron Lines in Active Galactic Nuclei". In: *PASP* 112.775, pp. 1145–1161. DOI: 10.1086/316610. arXiv: astro-ph/0004366 [astro-ph].

Fabian, A. C., M. J. Rees, et al. (May 1989). "X-ray fluorescence from the inner disc in Cygnus X-1." In: *MNRAS* 238, pp. 729–736. DOI: 10.1093/mnras/238.3.729.

Fabian, A. C., D. R. Wilkins, et al. (July 2012). "On the determination of the spin of the black hole in Cyg X-1 from X-ray reflection spectra". In: *MNRAS* 424.1, pp. 217–223. DOI: 10.1111/j.1365-2966.2012.21185.x. arXiv: 1204.5854 [astro-ph.HE].

Farr, Will M. et al. (Nov. 2011). "The Mass Distribution of Stellar-mass Black Holes". In: *ApJ* 741.2, 103, p. 103. DOI: 10.1088/0004-637X/741/2/103. arXiv: 1011.1459 [astro-ph.GA].

Finkelstein, David (May 1958). "Past-Future Asymmetry of the Gravitational Field of a Point Particle". In: *Physical Review* 110.4, pp. 965–967. DOI: 10.1103/PhysRev.110.965.

Garcia, J., T. Dauser, A. Lohfink, et al. (2014). "Improved Reflection Models of Black Hole Accretion Disks: Treating the Angular Distribution of X-Rays". In: *ApJ* 782, p. 76. DOI: 10.1088/0004-637X/782/2/76.

Garcia, J., T. Dauser, C. S. Reynolds, et al. (2013). "X-ray reflected spectra from accretion disk models. III. A complete grid of ionized reflection calculations". In: *ApJ* 768, p. 146. DOI: 10.1088/0004-637X/768/2/146.

Garcia, J. and T. R. Kallman (2010). "X-Ray Reflected Spectra from Accretion Disk Models. I. Constant Density Atmospheres". In: *ApJ* 718, p. 695. DOI: 10.1088/0004-637X/718/2/695.

García, Javier A., Thomas Dauser, et al. (Feb. 2022). "Relativistic X-Ray Reflection Models for Accreting Neutron Stars". In: *ApJ* 926.1, 13, p. 13. DOI: 10.3847/1538-4357/ac3cb7. arXiv: 2111.12838 [astro-ph.HE].

García, Javier A., James F. Steiner, et al. (Nov. 2015). “X-Ray Reflection Spectroscopy of the Black Hole GX 339–4: Exploring the Hard State with Unprecedented Sensitivity”. In: *ApJ* 813.2, 84, p. 84. DOI: 10.1088/0004-637X/813/2/84. arXiv: 1505.03607 [astro-ph.HE].

Gatuzz, E. et al. (Jan. 2019). “Chandra high-resolution spectra of 4U 1630-47: the disappearance of the wind”. In: *MNRAS* 482, pp. 2597–2611. DOI: 10.1093/mnras/sty2850. eprint: 1810.09464.

George, I. M. and A. C. Fabian (Mar. 1991). “X-ray reflection from cold matter in Active Galactic Nuclei and X-ray binaries.” In: *MNRAS* 249, p. 352. DOI: 10.1093/mnras/249.2.352.

Goodman, J. and J. Weare (2010). “Ensemble samplers with affine invariance”. In: *Commun. Appl. Math. Comput. Sci.* 5, p. 65. DOI: 10.2140/camcos.2010.5.65.

Hawking, S. W. (June 1972). “Black holes in general relativity”. In: *Communications in Mathematical Physics* 25.2, pp. 152–166. DOI: 10.1007/BF01877517.

Heger, A., C. L. Fryer, et al. (July 2003). “How Massive Single Stars End Their Life”. In: *ApJ* 591.1, pp. 288–300. DOI: 10.1086/375341. arXiv: astro-ph/0212469 [astro-ph].

Heger, A. and S. E. Woosley (Mar. 2002). “The Nucleosynthetic Signature of Population III”. In: *ApJ* 567.1, pp. 532–543. DOI: 10.1086/338487. arXiv: astro-ph/0107037 [astro-ph].

Hjorth-Jensen, Morten (Aug. 2015). *Computational Physics: Lecture Notes Fall 2015*. URL: https://www.hlevkin.com/hlevkin/60numalgs/C/Hjorth-Jensen%20Computational%20Physics.pdf.

Hynes, Robert I. (2014). “Multiwavelength observations of accretion in low-mass X-ray binary systems”. In: *Accretion Processes in Astrophysics*. Ed. by Ignacio González Martínez-País, Tariq Shahbaz, and Jorge Casares Velázquez. Canary Islands Winter School of Astrophysics. Cambridge University Press, pp. 117–150.

Ingram, A. et al. (2019). “A public relativistic transfer function model for X-ray reverberation mapping of accreting black holes”. In: *MNRAS* 488, p. 324. DOI: 10.1093/mnras/stz1720.

Ingram, Adam R. and Sara E. Motta (Sept. 2019). “A review of quasi-periodic oscillations from black hole X-ray binaries: Observation and theory”. In: *New A Rev.* 85, 101524, p. 101524. DOI: 10.1016/j.newar.2020.101524. arXiv: 2001.08758 [astro-ph.HE].

Israel, Werner (Dec. 1967). “Event Horizons in Static Vacuum Space-Times”. In: *Physical Review* 164.5, pp. 1776–1779. DOI: 10.1103/PhysRev.164.1776.

Jebsen, J. T. (Jan. 1921). “On the General Spherically Symmetric Solutions of Einstein’s Gravitational Equations in Vacuo.” In: *Arkiv for Matematik, Astronomi och Fysik* 15.18, p. 18.

Jiang, J. et al. (2022). “Black hole spin measurements based on a thin disc model with finite thickness - I. An example study of MCG-06-30-15”. In: *MNRAS* 514, p. 3246. DOI: 10.1093/mnras/stac1369.

Johannsen, Tim (Aug. 2013). "Regular black hole metric with three constants of motion". In: *Phys. Rev. D* 88.4, 044002, p. 044002. DOI: 10.1103/PhysRevD.88.044002. arXiv: 1501.02809 [gr-qc].

Kalemci, E., M. Diaz Trigo, et al. (Nov. 2025). "Dust scattering halo of 4U 1630-47: high resolution X-ray and mm observations constrain source and molecular cloud distances". In: *MNRAS* 543.3, pp. 3073–3088. DOI: 10.1093/mnras/staf1688. arXiv: 2510.02879 [astro-ph.GA].

Kalemci, E., T. J. Maccarone, and J. A. Tomsick (May 2018). "A Dust-scattering Halo of 4U 1630–47 Observed with Chandra and Swift: New Constraints on the Source Distance". In: *ApJ* 859, p. 88. DOI: 10.3847/1538-4357/aabcd3.

Kallman, T. and M. Bautista (2001). "Photoionization and High-Density Gas". In: *ApJS* 133, p. 221. DOI: 10.1086/319184.

Kerr, Roy P. (Sept. 1963). "Gravitational Field of a Spinning Mass as an Example of Algebraically Special Metrics". In: *Phys. Rev. Lett.* 11.5, pp. 237–238. DOI: 10.1103/PhysRevLett.11.237.

King, A. L., J. M. Miller, et al. (2013). "WHAT IS ON TAP? THE ROLE OF SPIN IN COMPACT OBJECTS AND RELATIVISTIC JETS". In: *ApJ* 771, p. 84. DOI: 10.1088/0004-637X/771/2/84.

King, A. L., D. J. Walton, et al. (Mar. 2014). "The Disk Wind in the Rapidly Spinning Stellar-Mass Black Hole 4U 1630-472 Observed with NuSTAR". In: *ApJ Lett.* 784, p. L2. DOI: 10.1088/2041-8205/784/1/L2.

King, A. R. and U. Kolb (May 1999). "The evolution of black hole mass and angular momentum". In: *MNRAS* 305.3, pp. 654–660. DOI: 10.1046/j.1365-8711.1999.02482.x. arXiv: astro-ph/9901296 [astro-ph].

Kormendy, John and Douglas Richstone (Jan. 1995). "Inward Bound—The Search For Supermassive Black Holes In Galactic Nuclei". In: *ARA&A* 33, p. 581. DOI: 10.1146/annurev.aa.33.090195.003053.

Kuulkers, E. et al. (Feb. 1998). "Absorption Dips in the Light Curves of GRO J1655-40 and 4U 1630-47 during Outburst". In: *ApJ* 494, pp. 753–758. DOI: 10.1086/305248. eprint: astro-ph/9710024.

Laor, Ari (July 1991). "Line Profiles from a Disk around a Rotating Black Hole". In: *ApJ* 376, p. 90. DOI: 10.1086/170257.

Li, L.-X. et al. (2005). "Multitemperature Blackbody Spectrum of a Thin Accretion Disk around a Kerr Black Hole: Model Computations and Comparison with Observations". In: *ApJS* 157, p. 335. DOI: 10.1086/428089.

Li, Songcheng et al. (Sept. 2025). "Assessing the Power-Law Emissivity Assumption in X-ray Reflection Spectroscopy: A Simulation-Based Evaluation of Different Coronal Geometries". In: *arXiv e-prints*, arXiv:2509.20752, arXiv:2509.20752. DOI: 10.48550/arXiv.2509.20752. arXiv: 2509.20752 [astro-ph.HE].

Lindquist, R. W. (1966). "Relativistic transport theory". In: *Ann. Phys.* 37, p. 487. DOI: 10.1016/0003-4916(66)90207-7.

Liu, Honghui (2024). "Probing the Inner Accretion Flow around Black Holes with X-ray Observations". PhD thesis. Fudan University, China.

Liu, Honghui, Askar B. Abdikamalov, et al. (June 2019). "Testing the Kerr hypothesis using x-ray reflection spectroscopy with NuSTAR data of Cygnus X-1 in the soft state". In: *Phys. Rev. D* 99.12, 123007, p. 123007. DOI: 10.1103/PhysRevD.99.123007. arXiv: 1904.08027 [gr-qc].

Liu, Honghui, Cosimo Bambi, et al. (June 2023). "The Hard-to-soft Transition of GX 339-4 as Seen by Insight-HXMT". In: *ApJ* 950.1, 5, p. 5. DOI: 10.3847/1538-4357/acca17. arXiv: 2211.09543 [astro-ph.HE].

Liu, Honghui, Long Ji, et al. (Mar. 2021). "Testing Evolution of LFQPOs with Mass Accretion Rate in GRS 1915+105 with Insight-HXMT". In: *ApJ* 909.1, 63, p. 63. DOI: 10.3847/1538-4357/abdf65. arXiv: 2012.01825 [astro-ph.HE].

Liu, Honghui, Jiachen Jiang, et al. (July 2023). "High-density Reflection Spectroscopy of Black Hole X-Ray Binaries in the Hard State". In: *ApJ* 951.2, 145, p. 145. DOI: 10.3847/1538-4357/acd8b9. arXiv: 2303.10593 [astro-ph.HE].

Liu, Honghui, Haiyang Wang, et al. (June 2020). "Reflection Features in the X-Ray Spectrum of Fairall 9 and Implications for Tests of General Relativity". In: *ApJ* 896.2, 160, p. 160. DOI: 10.3847/1538-4357/ab917a. arXiv: 2004.11542 [gr-qc].

Madau, Piero, Francesco Haardt, and Massimo Dotti (Apr. 2014). "Super-critical Growth of Massive Black Holes from Stellar-mass Seeds". In: *ApJ* 784.2, L38, p. L38. DOI: 10.1088/2041-8205/784/2/L38. arXiv: 1402.6995 [astro-ph.CO].

Markoff, Sera, Michael A. Nowak, and Jörn Wilms (Dec. 2005). "Going with the Flow: Can the Base of Jets Subsume the Role of Compact Accretion Disk Coronae?" In: *The Astrophysical Journal* 635.2, p. 1203. DOI: 10.1086/497628. URL: https://doi.org/10.1086/497628.

Marra, L. et al. (Apr. 2024). "IXPE observation confirms a high spin in the accreting black hole 4U 1957+115". In: *A&A* 684, A95, A95. DOI: 10.1051/0004-6361/202348277. arXiv: 2310.11125 [astro-ph.HE].

McClintock, J. E., R. Narayan, and J. F. Steiner (2014). "Black Hole Spin via Continuum Fitting and the Role of Spin in Powering Transient Jets". In: *Space Science Reviews* 183, pp. 295–322.

McClintock, Jeffrey E. et al. (Nov. 2006). "The Spin of the Near-Extreme Kerr Black Hole GRS 1915+105". In: *ApJ* 652.1, pp. 518–539. DOI: 10.1086/508457. arXiv: astro-ph/0606076 [astro-ph].

Miller, M. Coleman and Jon M. Miller (2015). "The masses and spins of neutron stars and stellar-mass black holes". In: *Physics Reports* 548. The masses and spins of neutron stars and stellar-mass black holes, pp. 1–34. ISSN: 0370-1573. DOI: https://doi.org/10.1016/j.physrep.2014.09.003. URL: https://www.sciencedirect.com/science/article/pii/S0370157314003160.

Mirzaev, T., C. Bambi, et al. (2024). "X-Ray Spectra of Black Hole X-Ray Binaries with Returning Radiation". In: *ApJ* 976, p. 229. DOI: 10.3847/1538-4357/ad8a63.

Mirzaev, T., S. Riaz, et al. (2024). "Toward More Accurate Synthetic Reflection Spectra: Improving the Calculations of Returning Radiation". In: *ApJ* 965, p. 66. DOI: 10.3847/1538-4357/ad303b.

Mirzaev, Temurbek (2025). "X-ray Reflection with Returning Radiation: Improvements with the ZIJI Model". PhD thesis. Fudan University, China.

Motta, S. E., T. M. Belloni, et al. (Jan. 2014). "Precise mass and spin measurements for a stellar-mass black hole through X-ray timing: the case of GRO J1655-40". In: *MNRAS* 437.3, pp. 2554–2565. DOI: 10.1093/mnras/stt2068. arXiv: 1309.3652 [astro-ph.HE].

Motta, S. E., T. Munoz-Darias, et al. (Mar. 2014). "Black hole spin measurements through the relativistic precession model: XTE J1550-564." In: *MNRAS* 439, pp. L65–L69. DOI: 10.1093/mnrasl/slt181. arXiv: 1312.3114 [astro-ph.HE].

Newman, E. T. et al. (June 1965). "Metric of a Rotating, Charged Mass". In: *Journal of Mathematical Physics* 6.6, pp. 918–919. DOI: 10.1063/1.1704351.

Niedzwiecki, A., M. Szanecki, and A. A. Zdziarski (2019). "Improved spectral models for relativistic reflection". In: *MNRAS* 485, p. 2942. DOI: 10.1093/mnras/stz487.

Niedzwiecki, A. and A. A. Zdziarski (2018). "The lamppost model: effects of photon trapping, the bottom lamp, and disc truncation". In: *MNRAS* 477, p. 4269. DOI: 10.1093/mnras/sty873.

Niedzwiecki, A., A. A. Zdziarski, and M. Szanecki (2016). "On the Lamppost Model of Accreting Black Holes". In: *ApJ Lett.* 821, p. L1. DOI: 10.3847/2041-8205/821/1/L1.

Niedzwiecki, A. and P. T. Zycki (2008). "On the variability and spectral distortion of fluorescent iron lines from black hole accretion discs". In: *MNRAS* 386, p. 759. DOI: 10.1111/j.1365-2966.2008.12735.x.

Nordström, G. (Jan. 1918). "On the Energy of the Gravitation field in Einstein's Theory". In: *Koninklijke Nederlandse Akademie van Wetenschappen Proceedings Series B Physical Sciences* 20, pp. 1238–1245.

Novikov, I. D. and K. S. Thorne (Jan. 1973). "Astrophysics of black holes." In: *Black Holes (Les Astres Occlus)*. Ed. by C. Dewitt and B. S. Dewitt, pp. 343–450.

Page, D. N. and K. S. Thorne (1974). "Disk-Accretion onto a Black Hole. Time-Averaged Structure of Accretion Disk". In: *ApJ* 191, p. 499. DOI: 10.1086/152990.

Pahari, M. et al. (2018). "AstroSat and Chandra View of the High Soft State of 4U 1630–47 (4U 1630–472): Evidence of the Disk Wind and a Rapidly Spinning Black Hole". In: *ApJ* 867, p. 86. DOI: 10.3847/1538-4357/aae53b.

Pasham, Dheeraj R., Tod E. Strohmayer, and Richard F. Mushotzky (Sept. 2014). "A 400-solar-mass black hole in the galaxy M82". In: *Nature* 513.7516, pp. 74–76. DOI: 10.1038/nature13710. arXiv: 1501.03180 [astro-ph.HE].

Penrose, R. (Feb. 1965). "Zero Rest-Mass Fields Including Gravitation: Asymptotic Behaviour". In: *Proceedings of the Royal Society of London Series A* 284.1397, pp. 159–203. DOI: 10.1098/rspa.1965.0058.

Penrose, Roger (Jan. 1969). "Gravitational Collapse: the Role of General Relativity". In: *Nuovo Cimento Rivista Serie* 1, p. 252.

Reissner, H. (Jan. 1916). "Über die Eigengravitation des elektrischen Feldes nach der Einsteinschen Theorie". In: *Annalen der Physik* 355.9, pp. 106–120. DOI: 10.1002/andp.19163550905.

Remillard, Ronald A. and Jeffrey E. McClintock (Sept. 2006). "X-Ray Properties of Black-Hole Binaries". In: *ARA&A* 44.1, pp. 49–92. DOI: 10.1146/annurev.astro.44.051905.092532. arXiv: astro-ph/0606352 [astro-ph].

Reynolds, C. S. (2021). "Observational Constraints on Black Hole Spin". In: *ARA&A* 59, p. 117. DOI: 10.1146/annurev-astro-112420-035022.

Reynolds, Christopher S. (Sept. 2014). "Measuring Black Hole Spin Using X-Ray Reflection Spectroscopy". In: *Space Sci. Rev.* 183.1-4, pp. 277–294. DOI: 10.1007/s11214-013-0006-6. arXiv: 1302.3260 [astro-ph.HE].

Riaz, S., D. Ayzenberg, et al. (2020a). "Modeling Bias in Supermassive Black Hole Spin Measurements". In: *ApJ* 895, p. 61. DOI: 10.3847/1538-4357/ab89ab.

— (2020b). "Reflection spectra of thick accretion discs". In: *MNRAS* 491, p. 417. DOI: 10.1093/mnras/stz3022.

Riaz, S., T. Mirzaev, et al. (2023). "Impact of the returning radiation in current tests of the Kerr black hole hypothesis using X-ray reflection spectroscopy". In: *Eur. Phys. J. C* 83, p. 838. DOI: 10.1140/epjc/s10052-023-12031-7.

Riaz, S., M. Szanecki, et al. (2021). "Impact of the Returning Radiation on the Analysis of the Reflection Spectra of Black Holes". In: *ApJ* 910, p. 49. DOI: 10.3847/1538-4357/abe2a3.

Ross, R. R. and A. C. Fabian (2005). "A comprehensive range of X-ray ionized-reflection models". In: *MNRAS* 358, p. 211. DOI: 10.1111/j.1365-2966.2005.08797.x.

Salpeter, E. E. (Aug. 1964). "Accretion of Interstellar Matter by Massive Objects." In: *ApJ* 140, pp. 796–800. DOI: 10.1086/147973.

Schnittman, J. D. and J. H. Krolik (2009). "X-ray Polarization from Accreting Black Holes: The Thermal State". In: *ApJ* 701, p. 1175. DOI: 10.1088/0004-637X/701/2/1175.

Schwarzschild, K. (Jan. 1916). "On the Gravitational Field of a Mass Point According to Einstein's Theory". In: *Abh. Konigl. Preuss. Akad. Wissenschaften Jahre 1906,92, Berlin,1907* 1916, pp. 189–196.

Seifina, E., L. Titarchuk, and N. Shaposhnikov (2014). "Black Hole Mass Determination in the X-Ray Binary 4U 1630-47: Scaling of Spectral and Variability Characteristics". In: *ApJ* 789, p. 57. DOI: 10.1088/0004-637X/789/1/57.

Shakura, N. I. and R. A. Sunyaev (Jan. 1973). "Black holes in binary systems. Observational appearance." In: *A&A* 24, pp. 337–355.

Shapiro, S. L., A. P. Lightman, and D. M. Eardley (Feb. 1976). "A two-temperature accretion disk model for Cygnus X-1: structure and spectrum." In: *ApJ* 204, pp. 187–199. DOI: 10.1086/154162.

Shapiro, Stuart L. and Saul A. Teukolsky (1983). *Black holes, white dwarfs and neutron stars. The physics of compact objects*. DOI: 10.1002/9783527617661.

Shashank, S. et al. (2022). "Testing Relativistic Reflection Models with GRMHD Simulations of Accreting Black Holes". In: *ApJ* 938, p. 53. DOI: 10.3847/1538-4357/ac9128.

Shashank, Swarnim et al. (Jan. 2026). "Modeling Reflection Spectra of Super-Eddington X-Ray Sources". In: *ApJ* 996.1, 51, p. 51. DOI: 10.3847/1538-4357/ae2614. arXiv: 2407.12890 [astro-ph.HE].

Spera, Mario, Michela Mapelli, and Alessandro Bressan (Aug. 2015). "The mass spectrum of compact remnants from the PARSEC stellar evolution tracks". In: *MNRAS* 451.4, pp. 4086–4103. DOI: 10.1093/mnras/stv1161. arXiv: 1505.05201 [astro-ph.SR].

Steiner, James F. et al. (July 2024). "An IXPE-led X-Ray Spectropolarimetric Campaign on the Soft State of Cygnus X-1: X-Ray Polarimetric Evidence for Strong Gravitational Lensing". In: *ApJ* 969.2, L30, p. L30. DOI: 10.3847/2041-8213/ad58e4. arXiv: 2406.12014 [astro-ph.HE].

Tauris, T. M. and E. P. J. van den Heuvel (2006). "Formation and evolution of compact stellar X-ray sources". In: *Compact stellar X-ray sources*. Ed. by Walter H. G. Lewin and Michiel van der Klis. Vol. 39, pp. 623–665. DOI: 10.48550/arXiv.astro-ph/0303456.

Thorne, K. S. and R. H. Price (Feb. 1975). "Cygnus X-1: an interpretation of the spectrum and its variability." In: *ApJ* 195, pp. L101–L105. DOI: 10.1086/181720.

Thorne, Kip S. (July 1974). "Disk-Accretion onto a Black Hole. II. Evolution of the Hole". In: *ApJ* 191, pp. 507–520. DOI: 10.1086/152991.

Tomsick, J. A. and P. Kaaret (July 2000). "X-Ray Spectral and Timing Evolution during the Decay of the 1998 Outburst from the Recurrent X-Ray Transient 4U 1630-47". In: *ApJ* 537, pp. 448–460. DOI: 10.1086/308999. eprint: astro-ph/0002084.

Tomsick, J. A., I. Lapshov, and P. Kaaret (Feb. 1998). "An X-Ray Dip in the X-Ray Transient 4U 1630-47". In: *ApJ* 494, pp. 747–752. DOI: 10.1086/305240. eprint: astro-ph/9709214.

Tripathi, A., A. B. Abdikamalov, et al. (2021). "Impact of the Disk Thickness on X-Ray Reflection Spectroscopy Measurements". In: *ApJ* 913, p. 129. DOI: 10.3847/1538-4357/abf6c5.

Tripathi, A., S. Nampalliwar, et al. (2019). "Toward Precision Tests of General Relativity with Black Hole X-Ray Reflection Spectroscopy". In: *ApJ* 875, p. 56. DOI: 10.3847/1538-4357/ab0e7e.

Tripathi, A., Y. Zhang, et al. (2021). "Testing General Relativity with NuSTAR Data of Galactic Black Holes". In: *ApJ* 913, p. 79. DOI: 10.3847/1538-4357/abf6cd.

Tripathi, A., B. Zhou, et al. (Nov. 2020). "Testing the Keplerian disk hypothesis using X-ray reflection spectroscopy". In: *Phys. Rev. D* 102, p. 103009. DOI: 10.1103/PhysRevD.102.103009.

Volonteri, Marta (July 2010). "Formation of supermassive black holes". In: *A&A Rev.* 18.3, pp. 279–315. DOI: 10.1007/s00159-010-0029-x. arXiv: 1003.4404 [astro-ph.CO].

Walton, D. J. et al. (July 2016). "The Soft State of Cygnus X-1 Observed with NuSTAR: A Variable Corona and a Stable Inner Disk". In: *ApJ* 826.1, 87, p. 87. DOI: 10.3847/0004-637X/826/1/87. arXiv: 1605.03966 [astro-ph.HE].

Wang, Yanan et al. (Jan. 2021). "A Variable Ionized Disk Wind in the Black Hole Candidate EXO 1846-031". In: *ApJ* 906.1, 11, p. 11. DOI: 10.3847/1538-4357/abc55e. arXiv: 2010.14662 [astro-ph.HE].

Webster, B. Louise and Paul Murdin (Jan. 1972). "Cygnus X-1-a Spectroscopic Binary with a Heavy Companion ?" In: *Nature* 235.5332, pp. 37–38. DOI: 10.1038/235037a0.

Wilkins, D. R. et al. (2020). "Returning radiation in strong gravity around black holes: reverberation from the accretion disc". In: *MNRAS* 498, p. 3302. DOI: 10.1093/mnras/staa2566.

Wilms, J., A. Allen, and R. McCray (Oct. 2000). "On the Absorption of X-Rays in the Interstellar Medium". In: *ApJ* 542.2, pp. 914–924. DOI: 10.1086/317016. arXiv: astro-ph/0008425 [astro-ph].

Yukterez, Simon (2016). *Ergosphere and event horizons of a rotating black hole.* Wikimedia Commons. Animated GIF, CC BY-SA 4.0. URL: https://commons.wikimedia.org/wiki/File:Ergosphere_and_event_horizons_of_a_rotating_black_hole.gif.

Zel'dovich, Ya. B. (Sept. 1964). "The Fate of a Star and the Evolution of Gravitational Energy Upon Accretion". In: *Soviet Physics Doklady* 9, p. 195.

Zhang, S. N., Wei Cui, and Wan Chen (June 1997). "Black Hole Spin in X-Ray Binaries: Observational Consequences". In: *ApJ* 482.2, pp. L155–L158. DOI: 10.1086/310705. arXiv: astro-ph/9704072 [astro-ph].

Zhao, S. J. et al. (May 2024). "The bright black hole X-ray binary 4U 1543-47 during the 2021 outburst: A thick accretion disk inflated by high luminosity". In: *A&A* 685, A42, A42. DOI: 10.1051/0004-6361/202347718. arXiv: 2312.09632 [astro-ph.HE].

Zhou, Menglei et al. (Feb. 2020). "Modeling uncertainties in X-ray reflection spectroscopy measurements I: Impact of higher order disk images". In: *Phys. Rev. D* 101.4, 043010, p. 043010. DOI: 10.1103/PhysRevD.101.043010. arXiv: 1910.12494 [gr-qc].

Zilberman, Noa (Aug. 2025). *Stealing Energy from a Black Hole.* Accessed: 2026-01-28. URL: https://www.lbscience.org/en/2025/08/05/stealing-energy-from-a-black-hole/.